Journal of Astronomical Telescopes, Instruments, and Systems

AstronomicalTelescopes.SPIEDigitalLibrary.org

Ground calibration of the Astro-H (Hitomi) soft x-ray spectrometer

Megan E. Eckart
Joseph S. Adams
Kevin R. Boyce
Gregory V. Brown
Meng P. Chiao
Ryuichi Fujimoto
Daniel Haas
Jan-Willem den Herder
Akio Hoshino
Yoshitaka Ishisaki
Caroline A. Kilbourne
Shunji Kitamoto
Maurice A. Leutenegger
Dan McCammon
Kazuhisa Mitsuda
F. Scott Porter
Kosuke Sato
Makoto Sawada
Hiromi Seta
Gary A. Sneiderman
Andrew E. Szymkowiak
Yoh Takei
Makoto S. Tashiro
Masahiro Tsujimoto
Cor P. de Vries
Tomomi Watanabe
Shinya Yamada
Noriko Y. Yamasaki

Megan E. Eckart, Joseph S. Adams, Kevin R. Boyce, Gregory V. Brown, Meng P. Chiao, Ryuichi Fujimoto, Daniel Haas, Jan-Willem den Herder, Akio Hoshino, Yoshitaka Ishisaki, Caroline A. Kilbourne, Shunji Kitamoto, Maurice A. Leutenegger, Dan McCammon, Kazuhisa Mitsuda, F. Scott Porter, Kosuke Sato, Makoto Sawada, Hiromi Seta, Gary A. Sneiderman, Andrew E. Szymkowiak, Yoh Takei, Makoto S. Tashiro, Masahiro Tsujimoto, Cor P. de Vries, Tomomi Watanabe, Shinya Yamada, Noriko Y. Yamasaki, "Ground calibration of the Astro-H (Hitomi) soft x-ray spectrometer," *J. Astron. Telesc. Instrum. Syst.* **4**(2), 021406 (2018), doi: 10.1117/1.JATIS.4.2.021406.

SPIE.

Ground calibration of the Astro-H (Hitomi) soft x-ray spectrometer

Megan E. Eckart,[a,*] Joseph S. Adams,[a,b] Kevin R. Boyce,[c] Gregory V. Brown,[d] Meng P. Chiao,[a,b] Ryuichi Fujimoto,[e] Daniel Haas,[f] Jan-Willem den Herder,[f] Akio Hoshino,[g] Yoshitaka Ishisaki,[h] Caroline A. Kilbourne,[a] Shunji Kitamoto,[g] Maurice A. Leutenegger,[a,b] Dan McCammon,[i] Kazuhisa Mitsuda,[j] F. Scott Porter,[a] Kosuke Sato,[k] Makoto Sawada,[l] Hiromi Seta,[h] Gary A. Sneiderman,[c] Andrew E. Szymkowiak,[m] Yoh Takei,[j] Makoto S. Tashiro,[n] Masahiro Tsujimoto,[j] Cor P. de Vries,[f] Tomomi Watanabe,[a,o] Shinya Yamada,[h] and Noriko Y. Yamasaki[j]

[a]NASA Goddard Space Flight Center, X-ray Astrophysics Laboratory, Greenbelt, Maryland, United States
[b]University of Maryland, CRESST, Baltimore County, Maryland, United States
[c]NASA Goddard Space Flight Center, Systems Engineering Branch, Greenbelt, Maryland, United States
[d]Lawrence Livermore National Laboratory, Physics Division, Livermore, California, United States
[e]Kanazawa University, Faculty of Mathematics and Physics, Kakuma-machi, Kanazawa, Ishikawa, Japan, Japan
[f]SRON Netherlands Institute for Space Research, Utrecht, Netherlands
[g]Rikkyo University, Department of Physics, Toshima-ku, Tokyo, Japan
[h]Tokyo Metropolitan University, Department of Physics, Hachiogi, Tokyo, Japan
[i]University of Wisconsin-Madison, Department of Physics, Madison, Wisconsin, United States
[j]JAXA, Institute of Space and Astronautical Science, Chuo-ku, Sagamihara, Kanagawa, Japan
[k]Tokyo University of Science, Department of Physics, Shinjuku-ku, Tokyo, Japan
[l]Aoyama Gakuin University, Department of Physics and Mathematics, Chuo-ku, Sagamihara, Kanagawa, Japan
[m]Yale University, Department of Physics, New Haven, Connecticut, United States
[n]Saitama University, Sakura-ku, Saitama, Japan
[o]University of Maryland, CRESST, College Park, Maryland, United States

Abstract. The Astro-H (Hitomi) Soft X-ray Spectrometer (SXS) was a pioneering imaging x-ray spectrometer with 5 eV energy resolution at 6 keV. The instrument used a microcalorimeter array at the focus of a high-throughput soft x-ray telescope to enable high-resolution nondispersive spectroscopy in the soft x-ray waveband (0.3 to 12 keV). We present the suite of ground calibration measurements acquired from 2012 to 2015, including characterization of the detector system, anti-coincidence detector, optical blocking filters, and filter-wheel filters. The calibration of the 36-pixel silicon thermistor microcalorimeter array includes parameterizations of the energy gain scale and line-spread function for each event grade over a range of instrument operating conditions, as well as quantum efficiency measurements. The x-ray transmission of the set of five Al/polyimide thin-film optical blocking filters mounted inside the SXS dewar has been modeled based on measurements at synchrotron beamlines, including with high spectral resolution at the C, N, O, and Al K-edges. In addition, we present the x-ray transmission of the dewar gate valve and of the filters mounted on the SXS filter wheel (external to the dewar), including beryllium, polyimide, and neutral density filters. [DOI: 10.1117/1.JATIS.4.2.021406]

Keywords: x-ray spectroscopy; microcalorimeter; detectors; calibration.

Paper 17060SSP received Aug. 15, 2017; accepted for publication Feb. 22, 2018; published online Apr. 13, 2018.

1 Introduction

The Hitomi mission,[1,2] formerly known as Astro-H, was launched from Tanegashima Space Center, Japan, on February 17, 2016. It carried the Soft X-ray Spectrometer (SXS),[3] a microcalorimeter array cooled to 50 mK to provide high-resolution nondispersive spectroscopy from 0.3 to 12 keV. The instrument enabled plasma diagnostics in this waveband, which includes the K-shell transitions of all astrophysically abundant elements from C through Ni, as well as the L-shell transitions of several elements, including Fe. The SXS was commissioned shortly after launch and began making astronomical measurements[4] just days into the mission.[5] The instrument performed as expected until the untimely loss of the mission on March 26, 2016.

The SXS microcalorimeter array[6] consisted of ion-implanted silicon thermistors and HgTe thermalizing x-ray absorbers that operate at a heat-sink temperature of 50 mK. Because of this low operating temperature, the optical path of the SXS included a set of five thin-film aluminized polyimide filters anchored to nested temperature stages. The filters shield the detector from long-wavelength thermal radiation from the instrument and optical and UV photons from the sky while allowing transmission in the soft x-ray waveband.[7]

The mission goals required a careful calibration of the SXS components prior to launch. In this article, we describe the calibration approach and ground calibration measurements: Sec. 2 provides an overview, Sec. 3 presents measurements related to the effective area, Sec. 4 discusses the detector system calibration, Sec. 5 describes the anti-coincidence (anti-co) detector calibration, Sec. 6 provides an overview of the timing calibration, and Sec. 7 provides a summary.

*Address all correspondence to: Megan E. Eckart, E-mail: Megan.E.Eckart@nasa.gov

2 Calibration Overview

The SXS ground calibration aimed to characterize the detector system performance over the relevant range of operating conditions and to measure the properties of the instrument used in calculating the effective area, primarily the x-ray transmission of the optical blocking filters and the quantum efficiency (QE) of the detector pixels. We worked to calibrate the instrument as well as possible to maximize the potential scientific returns, but at a minimum we met the following instrument calibration requirements:

- blocking filter transmission: knowledge to better than 5% at 0.5, 1.5, and 6 keV,
- detector QE: knowledge to better than 5% at 6 keV,
- line-spread function (core): knowledge of core line-spread function to $\Delta E_{FWHM} \pm 1$ eV,
- line-spread function (non-Gaussian component): understand non-Gaussian components so that in response to monochromatic light the number of counts in every 5 eV bin is known to within 1% of the peak bin,
- energy gain scale: knowledge of absolute energy to within ± 2 eV, and
- timing: knowledge of absolute event timing to within 10 ms.

We performed calibration measurements of the detector system at the highest level of instrument integration possible, in as flight-like an environment as possible. This approach was essential for measuring parameters sensitive to system noise or the dewar thermal environment. Detector parameters that do not exhibit such sensitivities were measured at the subsystem level, where there was less schedule pressure and access to a more extensive suite of x-ray generating calibration equipment. The SXS worked well at x-ray energies far higher than the primary science bandpass, and although the mirror effective area was small at high energies, dropping below 50 cm^2 at 15 keV, we performed a subset of the detector calibration measurements to 30 keV.

Our calibration work encompassed much more than a set of measurements of a complete flight instrument. Although our program generated prelaunch best estimates of the instrument calibration, providing the parameters that were used to interpret the astrophysics data, it also characterized and verified the components at various levels of development and integration. The characterization work was aimed at increasing our understanding of physical parameters and was used to shape our subsequent calibration campaigns. It enabled algorithm development to relate calibration data taken under one condition to the equivalent calibration for another condition. We performed verification checks of instrument performance at intermediate stages of development and integration to ensure the instrument was on track to comply with the noise budget. These were primarily checks of the detector noise and spectral resolution. On occasion these tests revealed an unexpected source of noise, for example, due to interference from other SXS or spacecraft subsystems, leading either to hardware changes to eliminate the noise or to a thorough characterization of the impact of the noise on the instrument performance.

Pilot calibration campaigns using the engineering model (EM) hardware preceded the measurements of the flight components. This work led to improvements in our calibration equipment and procedures, and, in the case of the EM blocking filter measurements, led to improvements of the final flight hardware, described in Sec. 3.1.1.

3 Effective Area Calibration

We combined measurements of the individual components in the optical path to calculate the prelaunch total instrument effective area. These components include the telescope and thermal shield plus hardware inside the SXS dewar. Here we present the calibration of components within the SXS dewar: the transmission of the optical blocking filters (Sec. 3.1) and the detector QE (Sec. 3.2). References 8–10 describe the soft x-ray telescope (SXT) calibration and total effective area.

We also calibrated the SXS components intended to be in the optical path at prescribed times only. We present the dewar gate valve Be window calibration in Sec. 3.3 and the transmission of the filter-wheel filters in Sec. 3.4.

3.1 *Optical Blocking Filters*

The SXS aperture contained a set of five aluminized polyimide blocking filters attached to different thermal stages of the instrument (see Table 1). The outer three filters had ~200-nm-thick films supported by silicon meshes micromachined using silicon-on-insulator (SOI) wafers. The films were attached to the meshes using epoxy. Each mesh consisted of a 208- or 225-micron-thick "coarse" hexagonal mesh with cell spacing of

Table 1 (Left columns) SXS dewar filter thermal interface, standard filter abbreviation, nominal operating temperature, and clear aperture diameter. See Ref. 7 for details. (Right columns) Thin-film component thicknesses and areal density of excess oxygen (σ) based on synchrotron calibration measurements. Polyimide is assumed to have the composition $C_{22}H_{10}N_2O_4$ and density 1.43 g cm^{-3}, as specified by Luxel Corp.

				Film thicknesses		σ
Interface	Filter abbreviation	Nominal temp. (K)	Clear aperture (mm)	Polyimide (Å)	Al (Å)	O (μg cm^{-2})
Calorimeter thermal sink	CTS	0.050	8.64	856	479	1.702
DA structure	DA	1.3	12.0	856	479	1.702
Inner vapor cooled shield	IVCS	28	18.5	1054	953	2.392
Outer vapor cooled shield	OVCS	150	24.0	979	1009	1.919
Dewar main shell	DMS	250	35.0	1025	923	2.327

Table 2 Optical blocking filter coarse and fine support mesh filling factor (f) and thickness (t); and epoxy maximum filling factor (f_{max}) and maximum thickness (t_{max}). The meshes are composed of silicon, with bar widths of 65 microns (coarse mesh) and ≈5 microns (fine mesh). The epoxy is modeled using the composition of polyimide as a proxy for the epoxy composition. Coarse mesh fill factors are based on microscopic measurements; fine mesh and epoxy fill factors are based on synchrotron measurements. The CTS and DA filters did not have support meshes.

	Coarse mesh		Fine mesh		Fine mesh epoxy	
Filter	f	t (μm)	f	t (μm)	f_{max}	t_{max} (μm)
IVCS	0.029	225	0.0282	25	0.0163	25.0
OVCS	0.029	225	0.0339	25	0.00997	12.1
DMS	0.029	208	0.0330	8	0.0220	8.0

5.28 mm within which there was an 8- or 25-micron-thick "fine" hexagonal mesh with cell spacing of 0.33 mm (see Table 2). The inner two filters used free standing films. The aperture assembly and filters are described in Ref. 7. The SXT image was sufficiently out of focus at the mesh filters—the beam from a point-source fills ∼9 mm of the 18.5-mm filter diameter for the IVCS filter—that our aim was to provide a best estimate of the spatially averaged total transmission rather than a two-dimensional map.

We measured the transmission of our 22 flight and flight-spare filters at Brookhaven National Laboratory's National Synchrotron Light Source (NSLS) in 2012 prior to integration into filter carriers. Figure 1 shows the filters readied for calibration at NSLS. We used beamlines X8A and U3C to constrain the broadband filter transmission; the K-shell edge fine structure of C, N, and O; and the fine support mesh filling fraction and epoxy filling fraction. (Sec. 3.1.1 describes our motivation for including a partial covering fraction of epoxy.) In addition, we made follow-up measurements of film witness samples at the Canadian Light Source (CLS) in 2015 to measure the Al K-edge fine structure and refine the C, N, and O edge measurements. Edge structure measurements were performed with energy spacing of ∼0.25 eV, whereas the broadband structure was measured with 5- to 50-eV spacing. The mesh filter measurements at NSLS were done with a 1.59-mm spot size, which is large enough to average over the fine mesh bars while missing the coarse mesh bars. Position scans prior to each calibration measurement ensured that the beam avoided the coarse mesh bars. For a subset of the filters we measured the transmission at several locations, confirming that the transmission was spatially uniform. We estimate an upper limit to the nonuniformity of 0.5%. Our EM calibration measurements (Sec. 3.1.1) showed that the process of integrating the filters into carriers did not change the x-ray transmission; we deemed similar measurements unnecessary for the flight filters. We derived the coarse mesh filling fraction using microscope measurements of the mesh bar-widths.

We modeled the broadband measurements of each of the 22 filters with free parameters for the polyimide thickness, Al thickness, and the surface oxide contamination on the Al and, for mesh-mounted filters only, fine mesh filling fraction, epoxy filling fraction, and epoxy thickness. The atomic broadband transmission models used cross sections from Ref. 11. For the C, N, and O K edge measurements, each edge was fit with an

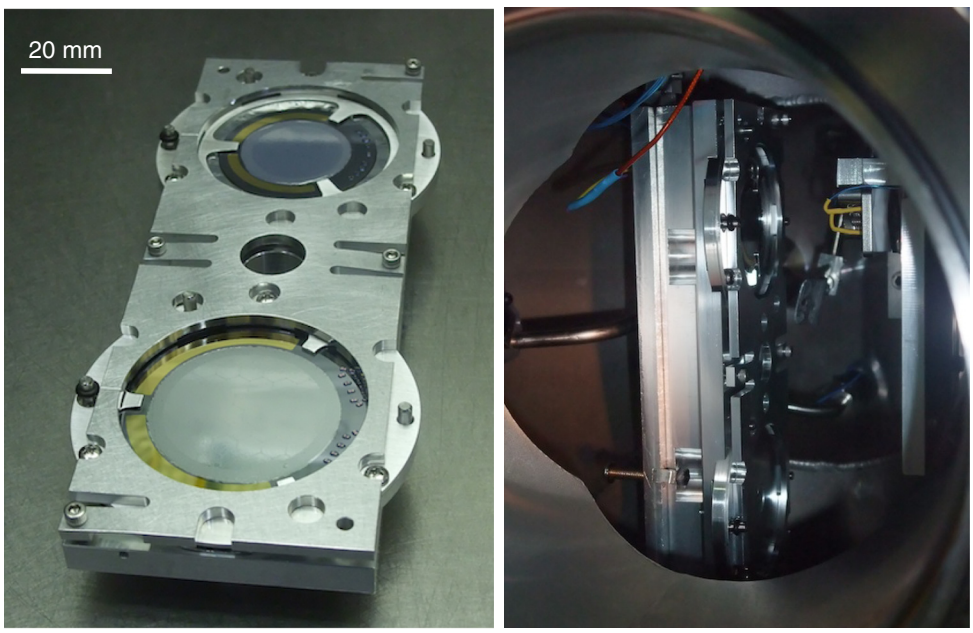

Fig. 1 (a) Two of the SXS optical blocking filters mounted in calibration holders at NSLS. (b) Filters in the endstation at NSLS beamline X8A. Monochromatic x-rays entered from the right.

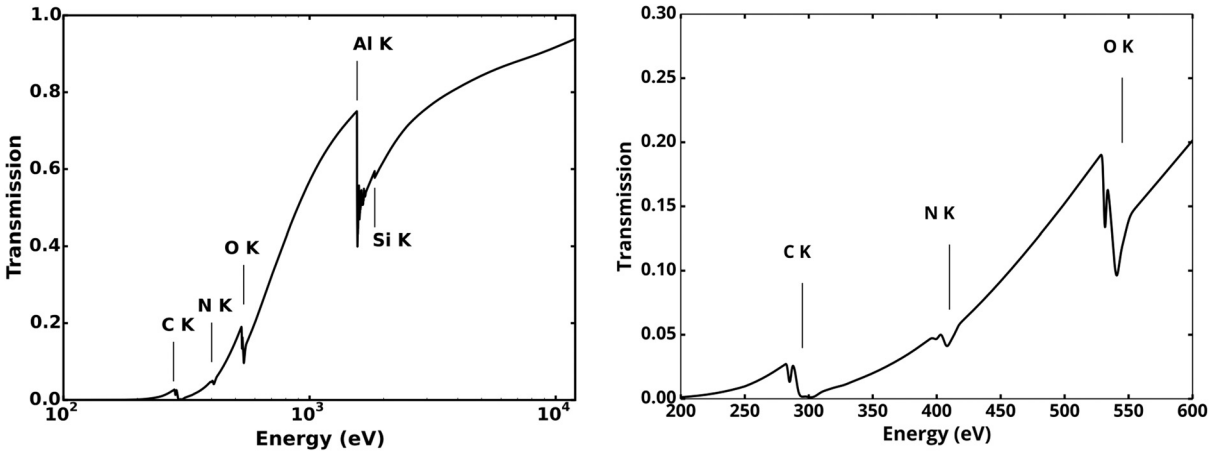

Fig. 2 Model of x-ray transmission of the set of five aluminized polyimide optical blocking filters (including detailed edge structure) constructed using the parameters in Tables 1 and 2. The zoomed plot at right highlights the fine structure at the C, N, and O K-edges.

empirical model consisting of a background pre-edge opacity, plus a sum of components each consisting of a Gaussian plus error function with fixed relative weight. The aluminum edge was not modeled; the data were used to directly interpolate the edge structure in the opacity. The fine mesh thickness was fixed to the specified value of 25 ± 0.5 μm for the IVCS and OVCS filters and 8 ± 0.5 μm for the DMS filter, which were confirmed to be within tolerance by direct measurements of representative meshes. Our epoxy model assumes a distribution of thicknesses, $0 < t < t_{\max}$, and a total filling fraction of epoxy, f. By conjecture, the distribution is $\frac{df}{dt} = c(t_{\max} - t)$, with the normalization requirement that $\int_0^{t_{\max}} \frac{df}{dt} dt = f$. This corresponds to a parabolic shape in the epoxy. Alternate distributions, including constant $\frac{df}{dt}$ (linearly sloped epoxy) and constant t, were also considered and could successfully reproduce the synchrotron data. We chose the parabolic distribution to best match the distribution seen via microscope inspections, but the resulting transmission is not significantly affected by the choice of model.

We performed all synchrotron measurements at room temperature, and our modeling does not include changes to the fine structure due to the operating temperature of each filter. Tables 1 and 2 show the best-fit film and mesh parameters. We estimate an uncertainty of ~0.2% in the per-filter broadband transmission, implying at most a 1% uncertainty in the transmission of a set of five dewar filters, assuming fully correlated errors. We prefer not to report individual uncertainties on the model parameters because of the significant covariance among the parameters; naively combining the uncertainties assigned to the individual parameters would significantly overestimate the uncertainty in the modeled total transmission. The filter transmission measurements and associated modeling, including of the K-edge structure, will be reported in greater detail in a forthcoming paper.

The coarse mesh thickness was assumed to be consistent with the specified value of 225 ± 5 μm (IVCS/OVCS) or 208 ± 5 μm (DMS), where the uncertainty lies primarily in the thickness of the 200-μm-thick handle layer. We neglected the buried oxide layer between the handle and device layers, which was specified at 0.5 μm $\pm$ 5% since it was thin compared with the tolerance on the handle layer thickness. These thicknesses were confirmed to be within tolerance by direct measurements of representative meshes.

The modeled transmissions for the five filters installed in the SXS dewar were combined with the coarse mesh measurements to produce the final calibration curve shown in Fig. 2. The right panel of Fig. 2 shows the detailed edge structure. At NSLS, we performed measurements of representative "stacks" of five filters in addition to measurements of the individual filters (see Fig. 3). The stacked measurements could not be used directly because the final set of filters installed in the instrument included what were considered flight spares at the time of the calibration campaign. But, these stacked measurements were successfully used as consistency checks of the individual measurements.

3.1.1 *Engineering model filter calibration: pilot calibration campaign, epoxy investigation, and contamination checks of filter–carrier integration process*

A pilot filters calibration program in 2011 preceded the final calibration campaign. We measured a set of five EM filters at NSLS on two separate runs, both before and after integration

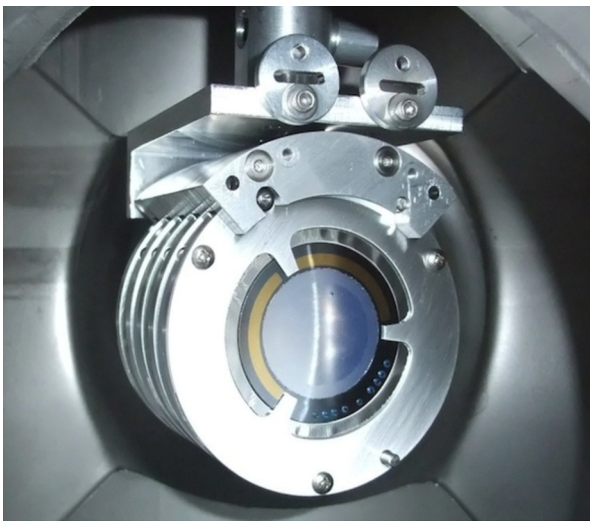

Fig. 3 Set of five SXS optical blocking filters readied for a "stacked" transmission measurement at NSLS.

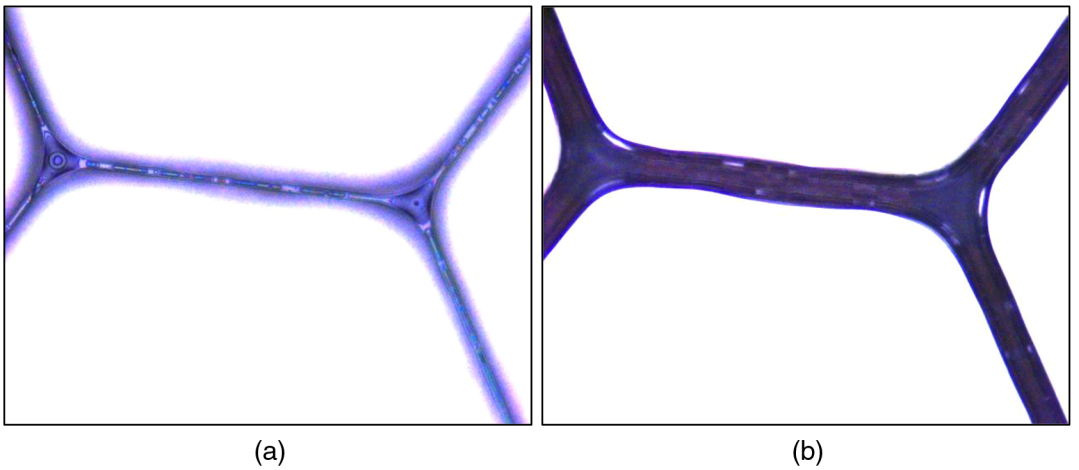

Fig. 4 Microscope image of the back of an EM optical blocking filter focused on the bottom of (a) the 5-μm-wide silicon mesh bars and (b) the filter film. The filter film appears white in these images. The excess epoxy, out of focus in the left image and in focus in the right image, bled beyond the fine-mesh silicon bars and significantly reduced the x-ray transmission at low energies. This effect was mitigated for the flight-model filters.

of the filters into filter carriers. These runs served several purposes: we developed procedures for the transmission measurements and the filter handling; we checked the filter transmission against the predicted transmission, which led to modification of the filter manufacturing procedure for the flight filters; and verified that the subsequent integration steps of the filters into their filter carriers did not change the x-ray transmission.

During the initial NSLS campaign, we determined an unexpectedly low transmission of the EM silicon-mesh filters at energies below 1.5 keV. The transmission was not well described by our models comprised of a silicon mesh plus uniform Al/poly film, and, in addition, the transmission was spatially nonuniform. We found that the data were well described when the model included a component describing a partial covering fraction of microns-thick low-Z material. Subsequent inspections of the EM filters under a high-powered microscope showed such a component: the epoxy used to attach the film to the mesh bled beyond the 5-μm-wide fine-mesh silicon bars (Fig. 4). The amount of epoxy bleed was not uniform across each filter (Fig. 5), again consistent with the NSLS finding of spatial nonuniformity. We worked with the manufacturer, who successfully modified the process and significantly reduced this effect without compromising the strength of the filters. For the Astro-H EM program Luxel used their standard "Epoxy Process Recipe 50" to attach the thin films to the Si meshes. The modified process developed for the flight filters is designated "Epoxy Process Recipe 30." The modeled epoxy covering fraction on the EM filters was 7% to 11%, whereas it was reduced to 1% to 2% for the flight filters, providing an increase in the low-energy transmission of a set of three mesh filters by, for example, 18% at 0.6 keV and 13% at 1.0 keV. This estimate was calculated assuming the best-fit epoxy distribution for the three measured EM filters with $f = 11.5\%$ (IVCS), 8% (OVCS), and 7.5% (DMS) and comparing to the three flight filters with $f = 1.6\%$ (IVCS), 1.0% (OVCS), and 2.2% (DMS). Based on the best-fit values the reduction in the total geometric filling fraction of the epoxy was 20% (=24.7-4.7%), with a distribution that was 90% opaque at 0.6 keV and ~65% opaque at 1.0 keV.

The integration of the silicon-mesh filters into their carriers and the CTS filter into the CTS box lid required the use of adhesives close to the filter films. We wanted to perform the flight filter calibration prior to such integration work for a number of reasons, primarily because the integrated hardware was bulky and difficult to mount in the beamline end stations and because damage to the fragile parts would have a smaller schedule and budget impact prior to integration, so we needed to verify that preintegration measurements would be valid. Our measurements of the set of EM filters both before and after integration showed that the x-ray transmission was identical to within our measurement uncertainty of 0.5% transmission in the 250 to 1000 eV band.

3.2 *Detector Quantum Efficiency and Filling Fraction*

The total SXS detector efficiency is a combination of the QE and filling fraction of the HgTe pixels, which were ~819 μm × 819 μm × 10.5 μm. We define the QE as the x-ray stopping

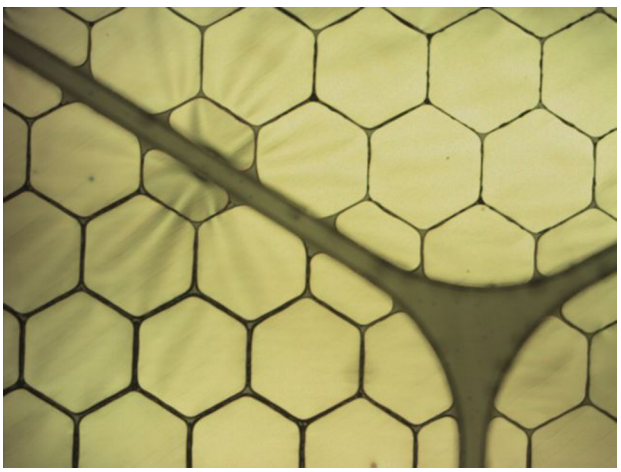

Fig. 5 Microscope image of the back of an EM optical blocking filter focused on the filter film and illustrating the nonuniformity of the excess epoxy, confirming the origin of the spatial nonuniformity in the EM x-ray transmission measurements. The bottom left shows a heavier epoxy compared to the top right.

Table 3 Absorber measurement summary. The absorbers are beveled such that the front surface is slightly larger than the back surface. The areal density of each absorber (right column) is calculated by dividing the mass of each absorber by the average absorber area midway between the two faces [$= (0.6711\ \text{mm}^2 + 0.66099\ \text{mm}^2)/2 = 0.666\ \text{mm}^2$].

	Area			
ID	Front surface [mm^2]	Back surface [mm^2]	Mass [μg]	Areal density [μg mm^{-2}]
5-2	0.67011		56.0	84.08
9-4	0.66908		57.7	86.63
5-8	0.67223		56.7	85.13
5-18	0.67227		57.2	85.88
6-18	0.67178		58.1	87.23
1-22		0.66204	56.7	85.13
1-21		0.65993	56.6	84.98
Average:	0.6711	0.66099		**85.6**
Std. dev.:	0.00128	0.00105		**1.0**

power of the pixels, which is determined by the x-ray absorber material (HgTe) and thickness. The absorber thickness and area were chosen to provide near-unity stopping power to energies of ≈6 keV and as high a filling fraction as was practical given the assembly constraints.[6]

The QE of each absorber as a function of incident x-ray energy can be described using $\text{QE}(E) = 1 - \exp[-\mu_{\text{HgTe}}(E)\Sigma]$, where $\mu_{\text{HgTe}}(E)$ is the mass absorption coefficient for HgTe and Σ is the areal density. The absorption coefficients for Hg and Te are known; assuming nominal stoichiometry of 1:1 we in turn know $\mu_{\text{HgTe}}(E)$ for the absorbers, using $\mu_{\text{HgTe}}(E) = [m_{\text{Hg}}\mu_{\text{Hg}}(E) + m_{\text{Te}}\mu_{\text{Te}}(E)]/(m_{\text{Hg}} + m_{\text{Te}})$, where m_{Hg} and m_{Te} are the atomic masses and $\mu_{\text{Hg}}(E)$ and $\mu_{\text{Te}}(E)$ are the mass absorption coefficients from the literature.[11] Neglecting uncertainty in the mass absorption coefficient, the uncertainty on the QE is given by $\sigma_{QE(E)} = \mu_{\text{HgTe}}[1 - \text{QE}(E)]\sigma_{\Sigma}$. The areal density is equivalent to the quantity $\rho * d$, where ρ is the density of the absorber and d is the thickness of the absorber, so assuming nominal HgTe density ($\rho = 8.17\ \text{g cm}^{-3}$),[12] the areal density provides an estimate of the absorber thickness.

The SXS QE was derived based on areal density measurements of seven spare HgTe absorbers from the same batch of absorbers used to construct the SXS detector array. The area of each absorber was measured by taking images using a microscope and attached cameras, which provided a resolution of 0.24 or 1.05 μm per camera pixel. Each absorber was then placed on a microbalance to obtain its mass. The dimensional measurements together with the mass measurements were used to calculate the areal density. Details of the measurements are shown in Table 3.

The high risk of damage to or breakage of an absorber during handling, in particular when removing an absorber from the microbalance, drove the use of spare absorbers over use of the absorbers slated for the flight detector array. The HgTe for all absorbers (flight and spare) was grown as a single continuous film and then etched into separate tiles prior to delivery to GSFC, and we expect negligible thickness variation among these absorbers. Our use of seven absorbers for areal density measurements was determined by the number of intact spare absorbers available.

The measurements of the spare absorbers indicate an areal density of $85.6 \pm 1\ \mu\text{g mm}^{-2}$, implying a thickness of $d \sim 10.5 \pm 0.1\ \mu$m. The quoted areal density is an average of the measurements of the seven spare absorbers. This average areal density is assumed for all SXS array pixels and thus a single QE value is calculated for the entire array (it is not a pixel-dependent QE). We adopt this approach since the variation in expected and measured pixel areal density is small and the areal density measurements cannot be made on the absorbers used for the flight instrument. The uncertainty on the areal density is dominated by uncertainty in the absorber mass. The uncertainty in the mass measurement is consistent with measurement error (uncertainty in the zero point of the balance of order 1 μg) in combination with some degree of nonuniformity at the beveled edge (chipping, etc.). We do not ascribe this uncertainty to a real variation in absorber density.

We used atomic scattering factor data for Hg and Te from 0.01 to 30 keV provided by the Center for X-ray Optics[11,13] (CXRO) to calculate the Hg and Te photoabsorption cross sections and mass attenuation coefficients, and interpolated these data to provide a step size of 0.25 eV. The interpolation was linear in $\mu E^{2.5}$, which was found to be well behaved. To provide a QE estimate for the extended bandpass (to 40 keV, where the SXS detector system performs well, but the mirror area is small), we extrapolated these data. For Hg, we fit the L-shell cross-section data from 25 to 30 keV with a power-law index, and used this function to extrapolate the data to 40 keV. To extrapolate the Te data to 40 keV, we again extrapolated based on a power-law fit to the L-shell cross section but also added the K-edge at 31.814 keV based on fits to data provided by NIST.[14–16] The Te mass attenuation coefficient data from 30 to 40 keV has the same functional form as the NIST data above 30 keV but is a factor of 1.083 higher, normalized to match the CXRO-provided data at 30 keV. Figure 6 presents plots of the calculated SXS QE and the associated fractional uncertainty.

The absorbers were placed on the 832-μm-pitch grid of the thermistor array. Because the HgTe absorbers were hand placed on the array, and thus had some variation in their positioning, we provided the positions of each pixel corner instead of an average fill fraction for the mission pipeline processing software calibration database.[17] This approach allows calculation of the size and position of each absorber and the gaps in-between. The fill fraction was 95.6%, ∼1% lower than that suggested by the typical absorber width of 819 μm and thermistor pitch due to an effective absorber pitch of ∼836.4 μm.

3.3 *Gate Valve Beryllium Window*

The SXS dewar gate valve housed a ∼300-μm-thick Be window that allowed x-ray transmission for energies above 2 keV while separating the instrument vacuum space from its surrounding environment. This architecture allowed x-ray testing and calibration on the ground, and on-orbit observations early in the spacecraft commissioning phase. We intended to open the gate valve at the end of the commissioning phase, ∼40 days into the mission, when the spacecraft outgassing rate was predicted to have been low enough to avoid contamination of the dewar optical blocking filters.[5] The x-ray transmission of the Be

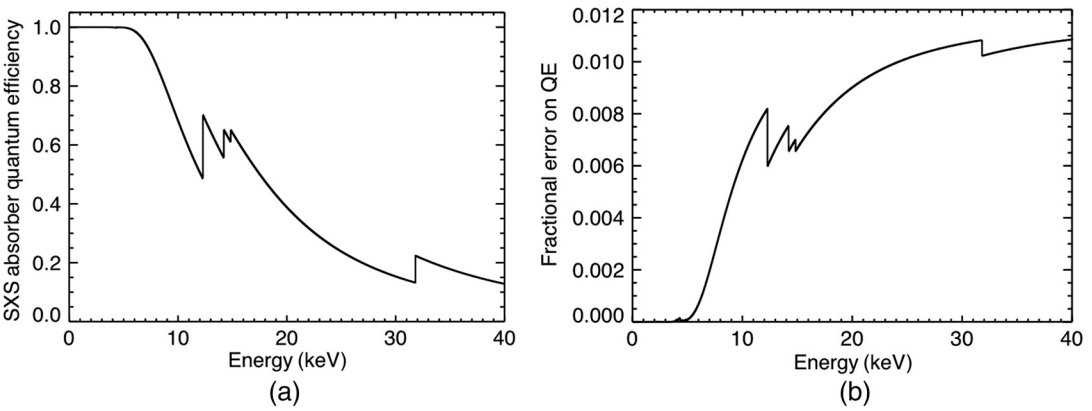

Fig. 6 (a) Absorption efficiency of the SXS array pixels, including the science (0.3 to 12 keV) and extended (12 to 40 keV) wavebands. The curve was calculated using the 85.6 μg mm^{-2} average measured areal density of the absorbers. (b) Fractional 1σ uncertainty on the QE due to the 1 μg mm^{-2} uncertainty in the areal density measurement. The uncertainty on the QE is <1% over the science bandpass.

window was not calibrated prior to launch due to a combination of schedule constraints and our intention to remove the window from the optical path prior to the on-orbit calibration and science observation phases. Instead, we calculated the transmission of the window based upon measurements of the flight-spare Be window and the nominal geometry and material properties of the metal support structures.

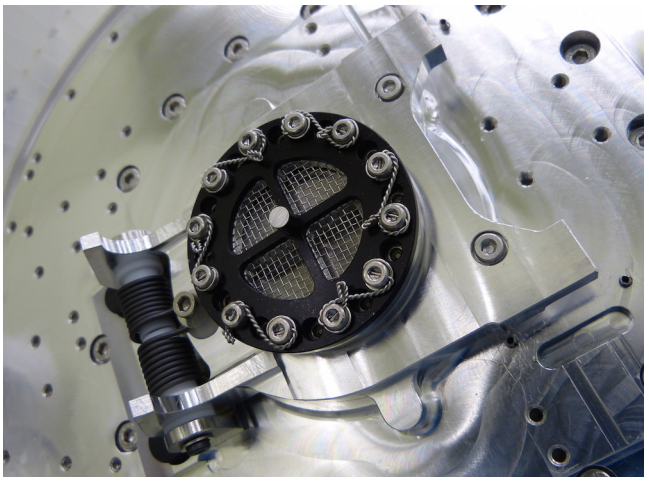

Fig. 7 Photo of the SXS dewar gate valve, highlighting the Be window and its support structures. The Be window sat just behind the protective stainless steel mesh.

The gate valve window, shown in Fig. 7, has a protective stainless mesh (71% open) and a thick support cross made of anodized Al, in addition to the Be window. Table 4 shows more information about these components. The target thickness for the gate valve Be window was 300 μm, but measurements of the flight window provided by the manufacturer, Materion Corp. (formerly Brush Wellman Ltd.), indicated a thickness in the range of 274 to 290 μm. (For reference, the difference in transmission of 274 μm-thick Be compared to 290 μm-thick Be is ~2% at 3 keV.) We do not have access to these data (methods, uncertainties, etc.) and thus previous estimates assumed the midpoint of this range, 282 μm.[18] Subsequently, we have measured the x-ray transmission of the flight-spare Be window, which was from the same lot of material as the flight Be window. Section 3.3.1 summarizes these measurements and Sec. 3.3.2 describes our approach to calculating the transmission of the flight gate valve assembly.

3.3.1 *Measurements of the flight-spare GV Be window*

In June 2016, x-ray transmission measurements were performed on the flight-spare Be window from 3.8 to 30 keV using beamline BL01B1 at SPring-8, a synchrotron operated by the Japan Synchrotron Radiation Research Institute. Here we provide a summary of the measurements and modeling results; Ref. 21 provides a detailed description. We used a beam spot size of 1 mm × 0.2 mm to measure two positions on the Be window, at the center of the Be window and at one position 6.5-mm

Table 4 Specification of SXS gate valve window components. Further details of the gate valve are available in the instrument calibration reports.[19,20]

Description	Material	Geometry	Thickness	Comment
Be window	Be	Uniform	~282 μm	No x-ray calibration measurements. See Table 5 for measurements of flight spare.
Protective mesh	Stainless steel: SUS304	1/20-in. pitch wire mesh	Wire thickness = 0.20 mm	Opaque in the SXS science waveband. Open fraction = 71%.
Support cross	Aluminum alloy: A6061-T6	Cross with 2-mm-wide bars	6 mm	Opaque in SXS science waveband. Aligned with SXT quadrant gaps.

off-center. Simultaneous transmission measurements of standard materials provided the energy calibration.

The transmission data clearly showed Fe and Ni K-edges, plus a marginal detection of the Mn K-edge. These features were expected based on the manufacturer's specifications. In addition, there were edge-like features observed at 6057 and 6915 eV, plus very weak edge-like features at 7590 and 9193 eV, which do not correspond to edge energies of any atomic absorption edges. The energies of these edges are consistent with the energies that correspond to the minimum allowed energy for Bragg diffraction from the $(1,-1,0,3)$, (0,0,0,4), $(1,0,-1,4)$, and $(1,0,-1,5)$ planes of Be. (The Bragg plane calculator[22] gives corresponding energies of 6060, 6918, 7588, and 9191 eV.) Above each energy Bragg diffraction is allowed for the corresponding plane. We posit that because the material is polycrystalline all Bragg angles and thus all diffracted energies are sampled, so that the effect looks like an edge in transmission. We caution that we have not performed calculations to verify if the relative edge strengths are reasonable and whether it makes sense to observe these edges and not others. Edges at the 2d for the $(2,-1,1,1)/5690$ eV, $(2,-1,1,0)/5420$ eV, and $(1,0,-1,2)/4665$ eV planes would be expected, but were not observed. The edge strengths may be too low for these features. Other potential edges in the science band of the SXS fall below the 3.8 keV minimum energy of the SPring-8 measurements, including scattering from the $(1,0,-1,1)/3575$ eV, $(0,0,0,2)/3460$ eV, and $(1,0,-1,0)/3129$ eV planes.

Our transmission data were best fit using the following components: photoabsorption by Be plus contaminants (Ni, Fe, Cu, Mn, Cr) using literature values of the mass absorption coefficients,[11] incoherent scattering by Be using μ_{inc} provided by Ref. 11, and edges at 6057 eV and 6915 eV that we ascribe to Bragg diffraction by the polycrystalline Be. For Be, the photoabsorption cross section dominates the total absorption cross section to ~7 keV, above which the contribution of incoherent scattering becomes significant. We calculate the contribution due to photoabsorption using $T(E) = \exp[-\mu(E)t]$ and incoherent scattering using $T(E) = \exp(-\rho\mu_{\mathrm{inc}}t)$, where $\mu(E)$ is the mass attenuation coefficient, t is the thickness, ρ is the density, and μ_{inc} is the cross section of incoherent scattering. We model the unknown edges using

$$T(E) = \begin{cases} 1 & \text{for } E < E_c \\ \exp\left[-D\left(\frac{E}{E_c}\right)^{-3}\right] & \text{for } E > E_c, \end{cases} \quad (1)$$

where D is the edge depth and E_c is the edge energy. The best-fit model parameters are presented in Table 5. The measurements at the two locations on the window were identical within error.

3.3.2 *Calculated transmission of the GV window*

We calculate the total transmission of the window by combining the effects of the three components listed in Table 4, but assuming the Be window itself is identical to that of the spare Be window (Table 5). We assume the Be is spatially uniform, and calculate an average transmission as a function of energy. Similarly, we provide an average transmission of the protective mesh; given the size of the converging x-ray beam from the telescope, the mesh geometry, and the size of the SXS detector pixels, a two-dimensional transmission map is not required. For both the Be window and stainless steel, we used literature atomic scattering factor data[11,13] from 0.01 to 30 keV to calculate the mass attenuation coefficients, and interpolated to 40 keV using a process similar to that described in Sec. 3.2. The stainless steel was assumed to have a composition of 70% Fe, 20% Cr, and 10% Ni. Within the SXS science bandpass, the mesh is opaque and simply reduces the window transmission by 29%. The support cross also attenuates a significant fraction of photons, despite being aligned with the telescope quadrants. To calculate the obscuration by the cross requires ray tracing using knowledge of the telescope parameters in addition to the detailed geometry of the SXS components. The ray-tracing calculations were performed by the Astro-H Software Calibration Team (SCT) that developed the mission software, with consistency checks performed by the SXT and SXS instrument teams. See Ref. 20 for details of the ray-tracing calculations. For a point source, the support cross attenuates ~23.3% of the photons across the science bandpass.

We present the combined transmission of the gate valve window components in Fig. 8. The metal support structures attenuate an approximately energy-independent 54% of the flux across the science bandpass. Figure 9 shows a zoom of the transmission from 5.8 to 9.2 keV, where the Bragg diffraction features and

Table 5 Best-fit Be window model parameters based on measurements of spare window. The errors represent 1-σ errors on the fits. We estimate an overall uncertainty of 1 μm in the Be thickness based on work to be presented in Ref. 23.

Element	Density [g cm^{-3}]	Best-fit thickness	Best-fit edge depth [$\times 10^{-3}$]	Comment
Be	1.85	261.86 ± 0.01 μm		Plus include incoherent scattering, with μ_{inc} from p. 305 of Ref. 11.
Cr	7.190	3 nm (fixed)		
Mn	7.30	3.81 ± 0.05 nm		
Fe	7.874	10.83 ± 0.05 nm		
Ni	8.902	16.48 ± 0.03 nm		
Cu	8.969	5 nm (fixed)		
6057 eV			2.194 ± 0.02	Attributed to Bragg scattering from polycrystalline Be
6915 eV			0.867 ± 0.03	Attributed to Bragg scattering from polycrystalline Be

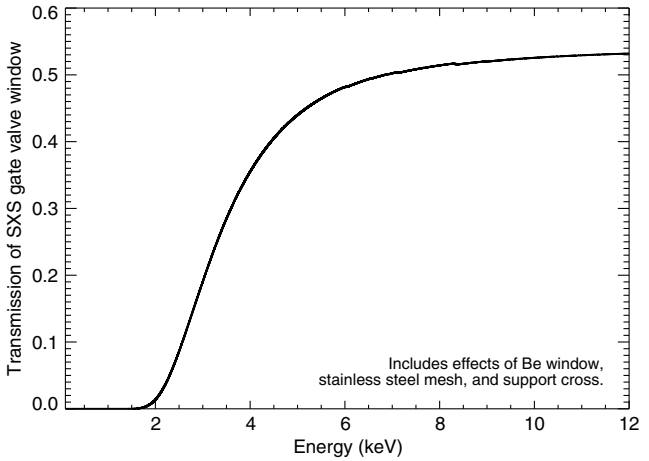

Fig. 8 Transmission of the gate valve window in the SXS science bandpass based on measurements of the flight-spare Be window.

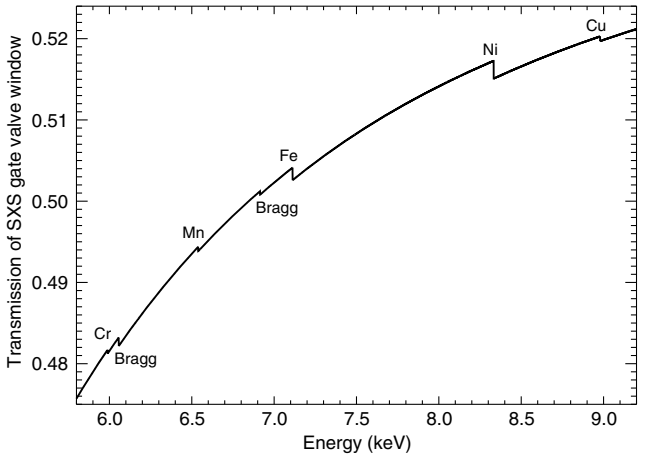

Fig. 9 Magnified version of the gate valve transmission curve in Fig. 8 with labels highlighting the Bragg diffraction features and atomic edges described in Table 5.

atomic edges due to contaminants are visible. Consistency checks of these estimates of the Be window transmission have been performed based on observations of astronomical sources from the mission commissioning phase.[10,24] Further refinements of our understanding of the transmission are in progress, in light of recent measurements of the flight-spare window at KEK that extend to 2 keV, revealing an additional Bragg scattering feature at ~3.5 keV.[23]

3.4 *Filter Wheel Filters*

The SXS had a filter wheel (FW) between the telescope and dewar aperture.[25] The wheel had six positions, which included two open positions. Table 6 shows an overview of the FW filters. While most observations would have been performed using an open position to ensure the maximum effective area, for certain objects, in particular for bright sources, observers might have inserted the neutral density filter or Be filter to reduce the source count rate at the detector.

Here we describe the measurements and calculations used to create the calibration curves presented in Fig. 10. Reference 20 describes the ray-tracing work used to calculate the effects of spatially varying structures.

3.4.1 *Polyimide filter*

We measured a flight-candidate polyimide filter at Berliner Elektronenspeicherring-Gesellschaft für Synchrotronstrahlung (BESSY) in January 2013. The measurements of the polyimide film were comprised of scans in energy from 0.2 to 1.9 keV with 50 eV step size at four positions on the filter, plus a measurement of the oxygen K-shell edge fine structure with 4 eV step size. Prior to each measurement, we performed a positional scan to ensure that the beam avoided the stainless steel mesh bars. We found that the broadband polyimide filter film transmission was well modeled using literature values of the polyimide mass attenuation coefficients[11,13] and a film thickness of 211 ± 3 nm, assuming polyimide composition $C_{22}H_{10}N_2O_4$ and density 1.43 g cm^{-3} as specified by the manufacturer, Luxel Corp. The measurements at different positions were identical within error, confirming spatial uniformity. We found that the O K-edge structure was consistent with the edge structure of the optical blocking filters measured at NSLS and CLS (Sec. 3.1).

Following a subsequent failure during vibration tests, the calibrated polyimide filter could not be used for flight, and a new polyimide filter was installed in the FW prior to spacecraft integration. There was not time in the schedule to calibrate the flight filter; instead, we assume the calibration measurements of the film properties from the damaged filter remained valid for the flight filter given the similarity in the film fabrication processes and manufacturer's specifications.

Table 6 Overview of SXS FW filters and the corresponding calibration measurements.

Filter position	Filter type	Purpose	Support geometry	Calibration measurement
1	Open	Default	n/a	n/a
2	Polyimide	Block contamination	Stainless steel mesh	Transmission at BESSY
3	Neutral density	Energy-independent attenuation of 24.5%	250-μm-thick Mo with 1.1 mm-diameter holes	Ray-trace based on drawing
4	Open	Default	n/a	n/a
5	Beryllium	Attenuate low-E photons	None	Transmission map at BESSY
6	^{55}Fe sources	Provide calibration lines on array	Cross	Ray-trace based on cross drawing

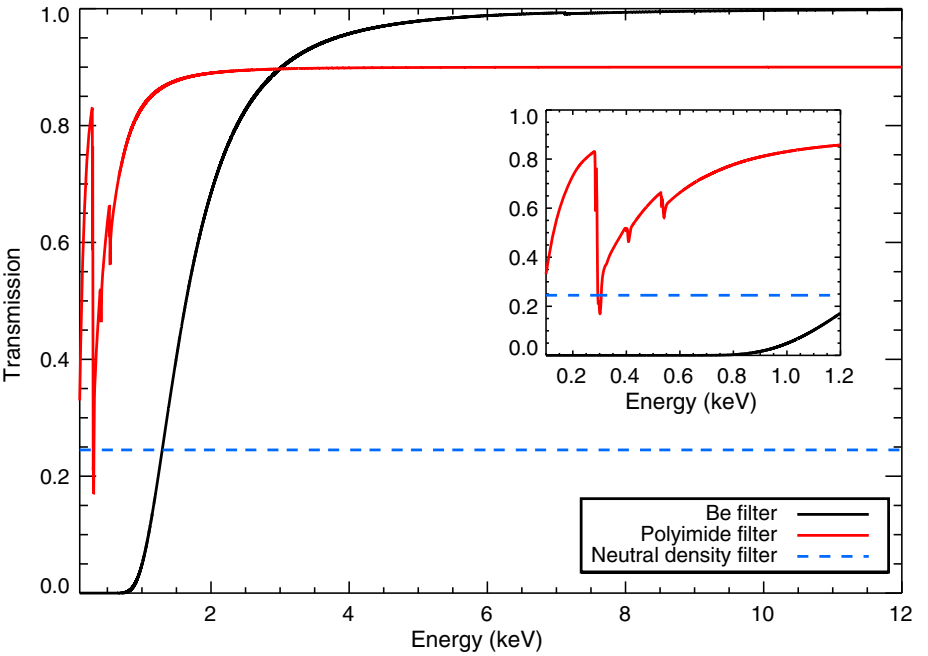

Fig. 10 Transmission of SXS FW filters across the science bandpass. The transmission of the Be filter shows a small decrement at 7.11 keV due to the Fe K-shell edge. The inset highlights the transmission at low energy, including the C, N, and O K-shell edges of the polyimide filter.

The support mesh for the polyimide filter was 0.25-mm thick and comprised of 70% Fe, 20% Cr, and 10% Ni. It had a 13.5% geometrical blocking factor without taking into account the telescope beam, but the effective blocking factor based on ray-trace simulations was found to be 10%.

We calculated the final prelaunch calibration curve by combining the 10% effective mesh blocking fraction with a polyimide transmission based on our blocking filters model assuming polyimide film thickness of 211 nm and including C, N, and O K-shell edge fine structure.

3.4.2 *Be filter*

We measured the x-ray transmission of two flight-candidate Be filters at BESSY in January 2013 from 0.2 to 10 keV with 50 eV step size at four positions on each filter. We also made high-resolution measurements over the energy range of the Fe K-shell edge from 7050 to 7200 eV with 2 eV step size at six positions, plus maps of each filter at 1.5 keV using a 45×45 spatial grid. The broadband transmission data were well fit assuming literature mass attenuation coefficients for Be[11,13] plus a small edge due to Fe impurities (0.2% average edge depth); the average thickness of the two filters was 25.5 and 28.3 μm. We used the spatial maps at 1.5 keV to calculate a map of Be thickness for each filter. These maps showed a standard deviation in thickness of $\sim$0.7 μm. We used the detailed maps in ray-tracing simulations to determine whether using an average filter transmission calibration curve rather than a two-dimensional transmission map was sufficient and found that using an average transmission did not introduce significant error.

Following damage to these calibrated flight-candidate filters in subsequent vibration tests, an uncalibrated qualification model Be filter was installed in the SXS FW.[25] The calibrated and uncalibrated filters were produced in the same batch and thus the material composition was likely to be the same, so we assumed the mass attenuation coefficients derived from the BESSY measurements remained valid. We also used the Be calibration results as a guide to the likely filter uniformity and thickness of the uncalibrated filter installed for flight.

We calculated the final prelaunch calibration curve (Fig. 10) assuming a Be thickness of 26.9 μm, the average of the thicknesses of the two measured filters, and the same level of Fe impurities.

3.4.3 *Neutral density filter*

Ray-tracing calculations[20] show that the transmission of the neutral density filter was 24.5% across the science bandpass, close to the targeted transmission of 25%. The transmission was slightly higher in the extended bandpass, with a maximum transmission of 28.4% at 20 keV near the Mo K-shell edge, based on calculations using the design Mo thickness (250 μm) and literature mass attenuation coefficients.[11]

3.4.4 *^{55}Fe mounting structure*

The effect of the mounting cross for the ^{55}Fe sources was calculated using the ray-tracing code.[20] The effect of the cross was energy dependent, blocking 3% to 10% of incident photons across the science bandpass, and had an increasing attenuation in the extended bandpass.

4 Detector System Calibration

The detector system calibration is important for a microcalorimeter spectrometer since it is the properties of the detector response that provide the spectral information. Our approach involved a thorough characterization of the detector system at multiple stages of integration—as a subsystem in a laboratory dewar at NASA's Goddard Space Flight Center (GSFC), after integration with the final flight cooling stages at GSFC, following integration into the flight dewar (in Japan), and after the

instrument was integrated onto the spacecraft. At each stage, we used the suite of x-ray generating calibration tools compatible with the testing configuration, which became more constrained as the level of integration increased.

Because the microcalorimeter pixels are very sensitive to their environment, we must understand how the calibration parameters change with, for example, changes in temperature of outer thermal shields or changes in the operational mode (nominal mode versus lifetime-extending cryogen-free mode[26]), so that using only limited line measurements onboard we may confidently calibrate the data over the full spectral range of the instrument.

In addition to instrument conditions, the detector calibration parameters depend upon the pulse processing method. Our data were acquired using the SXS pulse shape processor (PSP),[27–29] which calculated the pulse height of each event onboard using an optimal filter,[30,31] aside from cases where pulses are spaced very close in time (low-resolution or "lo-res" events). We calculated an optimal filter template for each pixel using x-ray pulse and noise data acquired when the instrument was fully integrated (but prior to installation on the spacecraft). Then, this set of templates was used for event processing for the entirety of the subsequent operations, including ground calibration and on-orbit observations. Reference 32 contains details of the PSP parameter settings used for the template generation and a description of how we derive templates for mid-resolution ("mid-res") event processing from the high-resolution ("hi-res") templates, as well as a description of the event grades themselves. In short, each triggered event is graded based on its relation in time to preceding and subsequent events on the same pixel, where events well separated in time (~80 ms) from surrounding events are deemed hi-res, events separated by ~20 to 80 ms are deemed mid-res, and lo-res events are separated by <20 ms. The mid-res and lo-res events are further divided into primaries or secondaries, denoting whether they are the leading or following events in the closely spaced group.

Here we describe the calibration tools used for detector system calibration in Sec. 4.1, followed by descriptions of the line-spread function (LSF) (Sec. 4.2) and energy gain scale (Sec. 4.3) calibration. We address the gain correction for mid-res secondaries (Sec. 4.3.4), but otherwise do not discuss the calibration of secondaries. The calibration at high count rate, which is primarily a function of the PSP behavior,[32] will be addressed in detail elsewhere as will the timing calibration;[33] however, we describe the relevant sources in Secs. 4.1.3 and 4.1.5 and provide brief summaries of the LSF at high count rate in Sec. 4.2.1 and the timing calibration in Sec. 6.

4.1 *Detector Calibration Equipment and On-Board Monitoring Sources*

4.1.1 *Monochromators for line-spread function characterization*

We measured the line-spread function for each detector pixel (Sec. 4.2) using several monochromators, the surface normal rotation grating monochromator (at energies below 2.5 keV), the double crystal monochromator (at energies above 4.5 keV), and newly developed portable channel-cut crystal monochromators (CCCMs) at 5.4 and 8.05 keV.

The surface normal rotation monochromator (SNR) generates monochromatic soft x-rays in the range 0.3 to 2.5 keV with energy resolution of 1 to 2 eV.[34] The x-rays are generated using a Manson source with changeable anodes, including carbon, stainless steel, copper, magnesium, aluminum, and gold. X-rays pass through an entrance slit and a collimating optic for the cross-dispersion direction, are diffracted from a reflection grating, which focuses the incident diverging beam at the exit slit, and then made monochromatic by the exit slit. The SNR illuminates the full SXS array, and it can generate at least five ct/s/pixel for any fluorescent line generated by the Manson source.

The double crystal monochromator (DCM) generates hard x-rays in the range 4.5 to 10 keV, with an energy resolution of 2 to 3 eV using Ge (111) crystals, and 0.3 to 0.7 eV using Si (400) crystals. The x-rays are generated by electron impact on targets mounted on a rotatable wheel. The x-rays then pass through an entrance slit and are reflected from one of the crystal pairs. The Ge (111) crystal illuminates the full array, but the Si (400) crystal only illuminates about one-third of the array and required multiple pointings. The count rates are no greater than 0.6 ct/s/pixel.

We recently developed low-cost high-resolution monochromators using channel-cut crystals.[35] A commercial x-ray tube illuminates a pair of channel-cut crystals that are aligned in a dispersive configuration to select the $K\alpha_1$ line of the anode material. For the LSF calibration, we used Si (220) channel-cut crystals with either a Cr- or Cu-anode Oxford x-ray tube to provide lines at 5.4 or 8.0 keV with an energy width of <0.5 eV FWHM. The output monochromatic beam provides a collimated image of the anode spot (typically 100 to 200 μm) in the dispersion direction, and is unfocused in the cross-dispersion direction, so that the source image in the detector plane appears as a line. The x-ray beam illuminates a single column of the SXS array at a time so we typically used a computer-controlled mechanical translation stage to sweep the position of the monochromator, providing even illumination across the array. Unlike the table-sized SNR and DCM, the CCCMs are small and can be hand carried by one person, and we were able to transport a CCCM from GSFC to testing facilities in Japan and safely mount it above the SXS dewar.

4.1.2 *Rotating target sources for gain scale characterization and core LSF measurements*

The rotating target source (RTS) generates line emission from 3.3 to 35 keV. We have two copies of this instrument, and typically had one at GSFC and the other at a testing facility in Japan. Each RTS consists of a bright x-ray continuum source (TruFocus model 5110 with tungsten target) that illuminates a series of eight thick, single-crystal targets mounted on a rotating wheel. Either manual or automated control of the rotating wheel is possible. Under automated control individual dwell times may be programmed for each individual target position. Fluorescence from the targets provides the necessary line emission across the energy band for energy scale calibration and checks of the LSF. The emission from the RTS simultaneously illuminates all pixels in the detector array.

We used a third RTS equipped for vacuum operation that provides fluorescent lines at lower energies (1 to 3 keV) during subsystem testing at GSFC. An Oxford x-ray tube with a Cr anode provides a bright x-ray continuum that illuminates a series of six targets mounted on a rotating wheel. Fluorescence from these targets provides a series of calibration lines. The space between the exit port of the Oxford tube, the target wheel, and the exit port to the dewar is enclosed in a vacuum chamber.

4.1.3 *High flux sources for calibration at high count rate*

The behavior of the SXS at high count rate was primarily related to the PSP, and depended upon details of how it triggered and processed (or omitted processing) events at incident rates above the ~200 ct/s/array count-rate limit (including unscreened events).[32] Each quadrant of the PSP read out a quarter of the 38 channels (36 calorimeter and 2 anti-co detector channels), and the count-rate limit per quadrant was ~50 ct/s. At high flux, to first order, the changes in the instrument data stream are in (1) the branching ratio (fewer hi-res events, more mid-res and lo-res events) and (2) the PSP's ability to process all of the events. Our primary purpose for the high flux measurements was to test the PSP, and these results will be described in a forthcoming paper. Other count-rate-related effects are described briefly in Sec. 4.2.1.

At GSFC, we performed a pilot calibration campaign at a high count-rate using the flight-spare detector assembly (DA) coupled to the PSP. We flood-illuminated the array with Mn K photons at rates up to 64 cts/s/pixel using the RTS and with Al K photons at rates of 10 cts/s/pixel using the vacuum RTS (Sec. 4.1.2), both operated in nonrotating mode. We simulated a point source at the center of the array at a series of fluxes, ranging from 20 to 80 cts/s/array, using a pinhole collimator at the dewar entrance aperture illuminated by an Oxford x-ray tube with Cr anode. This source configuration provided photons concentrated on 2×2 SXS pixels with the flux decreasing radially on surrounding pixels.

During instrument-level testing at Tsukuba Space Center, we again performed a series of measurements at high count rate with flood illumination and a simulated point source, although experiments at Al K were not possible because of the gate valve Be window. For the flood illumination, we used both the RTS and an EM modulated x-ray source (see Sec. 4.1.5). For the point-source simulation, we used the CCCM (Sec. 4.1.1) housing with the crystals removed. We mounted the Oxford x-ray tube with Cr anode to the CCCM housing and affixed a pinhole collimator to the exit port of the housing. The apparatus was mounted above the SXS and positioned using a computer-controlled translation stage; shims were used to tilt the housing so that the beam avoided vignetting by the GV support structure. This enabled exposures at high count rate on a 2×2 grid of array pixels, with the flux decreasing radially on surrounding pixels. We acquired data with the source aimed at the center of the array for count rates of 10, 20, and 40 cts/s/pixel on the most illuminated pixels, and offset experiments where the point source was centered on pixels read out by a single quadrant of the PSP.

4.1.4 *On-board sources*

There were multiple onboard calibration sources that could track time-varying changes in the detector gain and line-spread function. We used these sources to monitor the detector system during the ground testing and on orbit.

The primary, "always on," monitor was a dedicated calibration pixel. This pixel was offset from the main array pixels so that it was outside of the aperture but received a constant flux of photons from a small collimated ^{55}Fe source built into the lid of the detector box.[36] The Mn Kα line complex of the calibration pixel was used to monitor time-varying changes in the gain scale and the instrument resolution. We used the calibration pixel, pixel 12, at all stages of ground testing, from subsystem tests at GSFC to the day before launch.

There were two methods for flood-illuminating the array once the instrument was on the spacecraft, when we no longer were allowed to mount calibration equipment above the dewar. These onboard sources[25,37] could be used to check for or monitor offsets in gain between the calibration pixel and individual array pixels, as well as to monitor the spectral resolution of each pixel. First, there were the FW ^{55}Fe sources mounted on a metal structure that could be rotated into the optical path to illuminate the array. In addition, modulated x-ray sources (MXSs) were mounted on a fixed structure near the FW. Each MXS uses light-sensitive photocathodes to generate electrons, which impact an anode and in turn generate x-rays. The primary "direct" Astro-H MXS provided Cr K and Cu K emission lines and operated in a pulsed mode with duty cycles of ~1%. Thus, unlike the ^{55}Fe source, the MXS could have been operated during observations without affecting the instrument background since the calibration photons could be removed via timing cuts. A redundant MXS was mounted 180 degrees from the primary MXS.

The gate valve cross (Sec. 3.3) cast a shadow so that only a subset of the array pixels were illuminated by the MXS or FW ^{55}Fe sources during ground tests. We found that if we rotated the FW by 10 deg we were able to reduce the shadowing and illuminate all pixels with the ^{55}Fe sources. With the MXSs, only a few pixels on an outer column were well illuminated with the gate valve closed. Using the redundant MXS, we were able to illuminate a similar subset of pixels on the opposite side of the array.

4.1.5 *Sources for timing calibration*

For the timing calibration, we used an EM MXS unit operated with a laboratory power supply and arbitrary waveform generator as well as the onboard "direct" MXSs operated with flight electronics.[25] Signals from atmospheric muons, which are a background source of minimum-ionizing particle events, were used to establish relative timing between the anti-co and calorimeter pixels. To study pixel-to-pixel event correlation, we also incorporated data from the RTSs and the onboard ^{55}Fe sources.

We used the EM MXS mounted directly above the dewar to perform relative pixel-to-pixel timing calibration (see Sec. 6) during the instrument-level calibration campaign at Tsukuba Space Center in March 2015. In this configuration, there was no significant shadowing by the gate valve support structure and we were able to produce high instantaneous fluxes at the detector compared with the configuration on the spacecraft, where the MXS is much farther from the detector. We acquired 4 h exposures with the LEDs pulsed at 100 Hz with duty cycle of 0.1% in both normal operating mode and with the PSP in forced mid-res mode (Sec. 4.3.2 describes forced mid-res mode).

4.2 *Line-Spread Function*

We used several monochromators (Sec. 4.1.1) to provide nearly monochromatic x-rays to characterize the line-spread function (LSF) of each SXS pixel across the science bandpass. Figure 11 provides examples of the line-spread function and components we have identified and characterized as a function of energy.

We find that the core of the LSF for a given pixel is Gaussian at every energy; at energies of above a few keV the shape is Gaussian down at least three orders of magnitude. A small fraction of events are redistributed to lower energies due to several

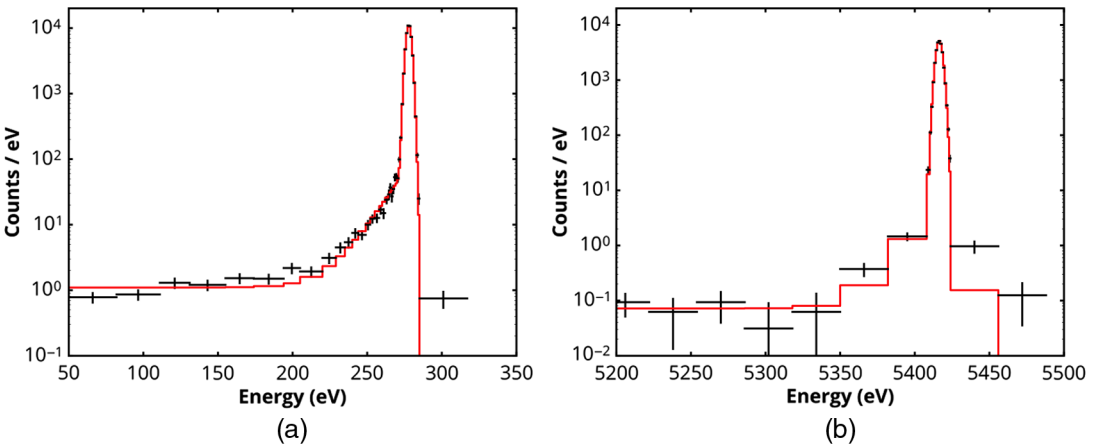

Fig. 11 (a) The line-spread function for a single SXS pixel in response to monochromatic x-rays at 282 eV. The black points are data measured during subsystem testing at GSFC in 2013. The red curve shows the LSF model, illustrating three components that we characterize as a function of incident x-ray energy: the Gaussian core, which dominates the line shape, an exponential tail to low energies, and the electron loss continuum. (b) LSF in response to monochromatic x-rays at 5.414 keV measured during subsystem testing at GSFC. At this energy, the LSF is well described by a Gaussian down over three orders of magnitude.

energy loss mechanisms, which we call the "extended LSF." These mechanisms include long-lived surface state excitations, giving rise to an exponential tail with e-folding of about 12 eV; scattering of photoelectrons out of the absorber, resulting in the so-called electron-loss continuum, which is empirically found to have roughly constant flux per unit energy interval; and x-ray fluorescence photons that may escape from the absorber instead of being thermalized, resulting in escape peaks. The Gaussian core depends on the detector and system noise, so the ground measurements serve as a guide, but must be re-measured on orbit. References 24 and 38 describe the on-orbit changes in the core LSF. The extended LSF resulting from events with partial energy loss should behave identically on the ground and on orbit.

4.2.1 *Gaussian core LSF*

Using both monochromatic and fluorescent line complexes, we find that the core Gaussian FWHM energy resolution for each pixel scales as a quadratic function of energy, with typical resolutions of order 4.5 eV FWHM at 6 keV and 5 eV FWHM at 8 keV for hi-res events during instrument testing prior to integration onto the spacecraft. The left panel of Fig. 12 shows an example of the core LSF as a function of energy for a single pixel and a quadratic fit to these data. The right panel of Fig. 12 shows the core LSF for each pixel at 5.9 keV and for baseline events. The baseline resolution data are derived from fits to histograms of baseline "events," which are the result of applying the PSP event-processing algorithm (optimal filter) in the absence of an x-ray signal. The baseline events, which were calculated at a regular interval during ground testing and on-orbit observations, provide an indication of the detector noise. In subsequent ground and on-orbit operations, we could use the baseline events to check whether the detector system performance had changed. We also used the baseline events to determine whether a change in measured resolution was consistent with the change in detector noise or whether it was due to a change in excess broadening, which is defined as $\sqrt{\Delta E^2 - \Delta E^2_{\mathrm{baseline}}}$.

The same procedure was used to measure the core LSF for mid-res primary and lo-res primary events. The core LSF at 5.9 keV for mid-res primaries was ~0.5 to 0.7 eV worse than the resolution for hi-res events shown in the right panel of Fig. 12, and the resolution for lo-res primaries was of order 15 eV. See Sec. 4.3.4 for a brief discussion of the energy resolution of mid-res secondaries.

The core LSF can be altered by nearest-neighbor electrical cross talk at high fluxes if x-ray events and cross-talk events occur at nearly the same time (within ±25 ms). During spacecraft-level ground tests, we found that during short, bright flashes from the MXS the resolution at Cu K was degraded due to cross talk from electrically adjacent pixels. The magnitude of the observed effect was confirmed via modeling and the degradation was eliminated if we instituted a pixel-to-pixel coincidence screening. Based on these results, we set a standard pixel-to-pixel coincidence screening in the software pipeline[39] to remove events that might be so affected, ensuring that the LSF broadening would be kept to <0.5 eV even with very high instantaneous fluxes. (The optimal filter is applied in the time domain and pulse height is computed from the correlation of a pulse record with the filter template. There was also enhanced sensitivity to crosstalk pulses that arrived in the last 2 ms of a pulse record due to non-zero power in the filter at the end of the template. This issue may be easily corrected for future missions via a minor change to the optimal filter template generation procedure.) The relative magnitude of thermal crosstalk is low,[40] and thus does not significantly affect the LSF of primary events even at high fluxes.

4.2.2 *Extended LSF*

We measured the extended LSF components during subsystem testing at GSFC in 2012 to 2013. Although we continue to refine both our models of the extended LSF and the suite of data, we present here our findings to-date.[41]

Exponential tail: We fit data acquired using monochromatic sources with the model described above to determine the fraction of counts in the exponential tail as a function of energy, and

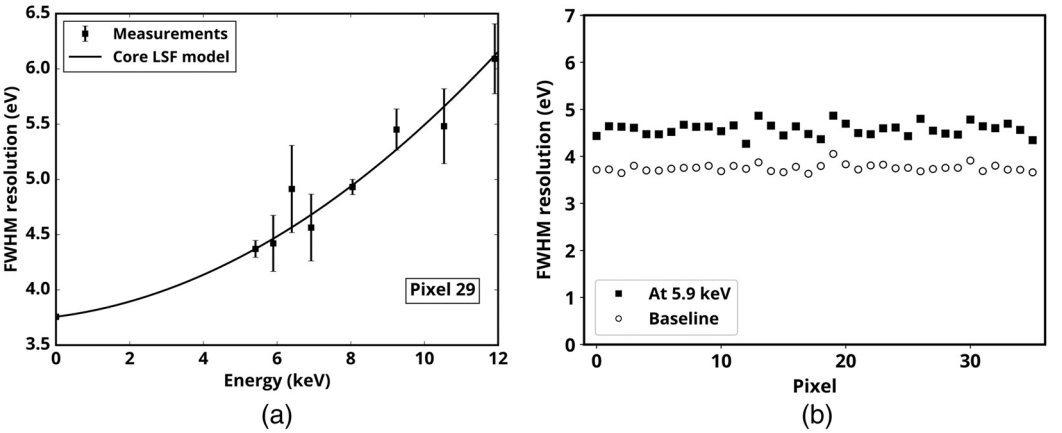

Fig. 12 (a) Measurements of the Gaussian core LSF of hi-res events on an SXS pixel as a function of energy. Data were acquired during the instrument-level calibration campaign at Tsukuba Space Center in March 2015. The data points at 5.4 and 8.0 keV with small error bars are fits to monochromatic lines; the other data points are fits to Kα line complexes generated with the RTS. We fit these measurements with a quadratic model. (b) Core LSF FWHM at 5.9 keV for hi-res events based on the quadratic fits to the measurements from 5 to 12 keV, as shown in the left panel, for each array pixel. We display the LSF at 5.9 keV to enable straightforward comparisons to subsequent LSF measurements using the onboard ^{55}Fe sources.[24,38] The baseline resolution is based on noise measurements and provides an indication of the best-achievable energy resolution in the absence of excess broadening.

find that the fraction changes significantly with energy. Where the tail is measurable, we find an e-folding that is consistent with ~12 eV for all incident x-ray energies. We hypothesize that the fraction of events in the tail is related to the penetration depth of the incident photon, and conjecture that this phenomenon has its origin in an unknown energy loss mechanism occurring preferentially near the surface of the absorber. Figure 13 shows the results for a single pixel, and compares the fraction of counts in the tail to the fraction of counts absorbed near the surface of the HgTe absorbers. We used literature values of the mass attenuation coefficient as described in Sec. 3.2 to calculate the absorption fraction for x-rays incident on a thin layer of HgTe, and adjusted the layer thickness until the absorption curve best matched the experimental data. The best fit was with 26 Å of HgTe. We use this relationship to interpolate the fraction of events falling in the tail for other incident energies. Although this model is consistent with the notion that the energy loss mechanism is related to trapping states due to altered band structure at the HgTe surface, it will be replaced by a more physically motivated model in our ongoing work.

Escape peaks and electron loss continuum: Fig. 14 provides an example of the escape peaks and electron loss continuum, which we measured using monochromators.

For the escape peaks, we estimate the expected strength of each peak relative to the main peak by calculating the penetration-depth-averaged escape probability from the HgTe absorber (taking into account absorption length of the incoming x-ray and the absorption length of the fluorescent photon, the latter assuming a uniform angular probability of emission), which was then multiplied by the fractional probability of creating the appropriate inner shell vacancy and the corresponding fluorescent yield and branching ratio. The calculation agrees with

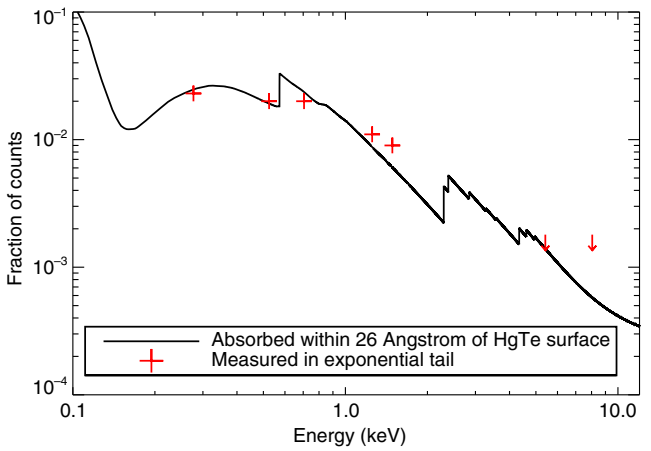

Fig. 13 Fraction of counts in the low-energy exponential tail of the SXS detector line-spread function (red symbols) based on data acquired using monochromators during subsystem tests at GSFC. The black curve shows the fraction of counts absorbed in the first 26 Å of the HgTe absorbers.

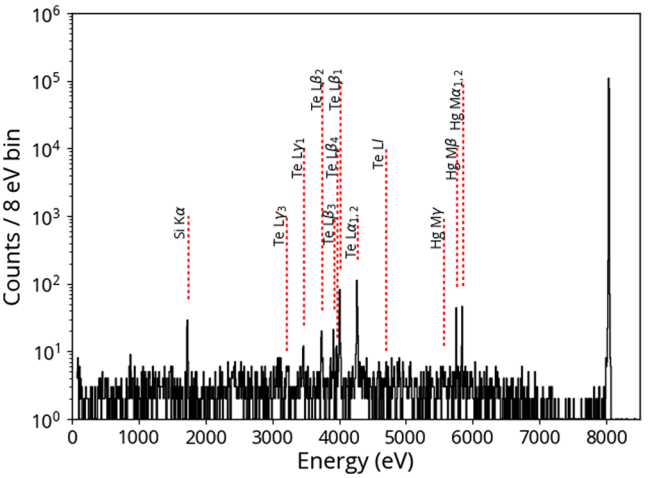

Fig. 14 Example of the electron loss continuum and escape peaks on a single SXS pixel using the Cu Kα_1 CCCM. Locations of Hg M and Te L escape peaks are marked. Si Kα fluorescence from the detector frame is also present.

the monochromator data for the strongest Hg M and Te L escape peaks,[41] and thus we used this model to interpolate the escape peak line strengths for incident energies other than those measured. The strength of the strongest Hg M escape peak ranges from 0.03% to 0.27% of the main peak, and similarly from 0.07% to 0.23% for the strongest Te L escape peaks.

Based on monochromator measurements, we approximate the electron loss continuum as flat in counts per unit energy bin. To estimate the appropriate fraction of events in the continuum as a function of incoming x-ray energy, we followed a procedure similar to that described for the escape peaks. We determined the penetration-depth-averaged escape probability of an electron from an HgTe absorber, averaged over the spectrum of photo- and Auger electrons for a given core vacancy, multiplied by the vacancy probability, and finally summed the spectra over all vacancies. The model predicts that 0.5% to 2% of events will be in the electron loss continuum for incident x-rays in the science bandpass, which is roughly consistent with measurements.

Silicon fluorescence: The Si Kα peak in Fig. 14 is the result of fluorescence from the detector frame. The line strength depends on the spectral and spatial distribution of the incident x-rays and has not been studied quantitatively. This feature was expected and observed in flight (e.g., see Fig. 4 and Table 2 of Ref. 10), but it was not included as a part of the extended LSF submitted to the mission calibration database. We planned to include it in subsequent versions of the calibration database by incorporating a model of the per-pixel fluorescence rate as a function of incident flux. For future missions, this will be included from the outset.

4.2.3 *Changes in LSF due to interference with spacecraft subsystems*

When operated on the spacecraft during ground testing, the core LSF was degraded by ~0.3 eV (a ~1.6 eV broadening term when added in quadrature), due to interference from the spacecraft attitude operations control system (AOCS), namely the reaction wheel (RW) and magnetic torquer (MTQ) subsystems. Figure 15 shows a detector noise spectrum from the spacecraft-level thermal vacuum tests in June 2015 at Tsukuba. We saw line noise on the detectors at 50 Hz due to interference from the RWs at 3000 RPM. Subsequent ground testing showed that this noise was produced by only one of the four reaction wheels (RW3), and moved in frequency with the rotation rate of RW3. We also saw interference at the MTQ pulse-width modulation frequency (127 Hz) and harmonics. The amplitude of these MTQ lines changed with the duty cycle settings but the frequencies remained the same. These effects are being investigated in detail based on ground tests and on-orbit data, and will be presented elsewhere. We introduce them here as an example of noise sources that change the core LSF due to changes in the baseline resolution.

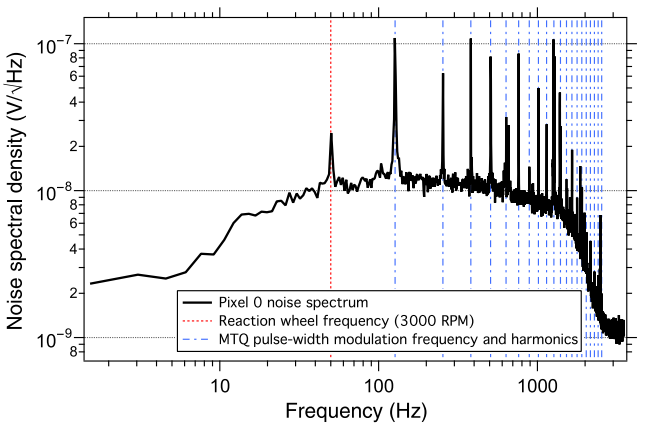

Fig. 15 Detector noise spectrum from SXS pixel 0 acquired during the spacecraft-level thermal vacuum test at Tsukuba in June 2015, showing an example of interference from the spacecraft that affects the noise level and core LSF. This noise changes in amplitude with MTQ setting and in both frequency and amplitude with RW setting. This example was acquired with AOCS settings that gave a relatively high level of interference.

4.3 *Energy Gain Scale*

4.3.1 *Overview and approach to energy gain scale calibration*

Many of the planned high-priority astrophysics investigations would be impossible without precise knowledge of the absolute energy of a given spectral feature. As a result, the knowledge of the SXS energy gain scale—the relationship between the measured signal and the incident photon energy—was essential, and the calibration requirement was a knowledge of the gain to within 2 eV across the science bandpass. Each pixel required its own gain correction, and the gain needed to be specified independently for each event grade.

The specific nature of any change in operating condition determined whether the corresponding gain change was linear (a stretch of the gain curve) or nonlinear (a change in shape of the gain curve). The gain of each SXS pixel depended linearly on the (small) gain–temperature coefficient of the room temperature amplifiers and had a nonlinear scaling with detector temperature. The detector temperature depended on the calorimeter thermal sink (CTS) temperature setpoint as well as loading on the control thermometers and detector pixels due to nearby structures such as the DA structure (~1.2 to 1.6 K) and the IVCS (~22 to 35 K). These effects tended to change the detector temperatures of all array pixels together. There was also differential radiative loading related to the screening of long-wavelength radiation that varied depending on pixel position in the array (i.e., inner pixels were better screened than outer pixels).

We measured the energy gain scale using the RTS from 4.5 to 13.5 keV. Fluorescence from the targets provided x-ray line emission directed to the instrument aperture. Calibration at low x-ray energies was not possible in the final instrument configuration due to the presence of the beryllium window on the dewar gate valve; however, the general shape of the low-energy gain was characterized during subsystem testing, and astrophysical calibration sources were going to be used to refine the low-energy gain scales. We measure the centroid of each line complex (in pulse-height space) and then fit the set of pulse height–energy pairs with a fourth-order polynomial; these polynomial coefficients define the gain curve and may be used for subsequent data analysis.

Based on analyses of gain curves measured over a wide span of instrument operating conditions, including in cryogen-free mode,[26] we found that we could treat all gain variations as equivalent to changes in detector temperature. Changes in detector temperature could be caused by, for example, a differential change in loading on the detector stage that resulted in a

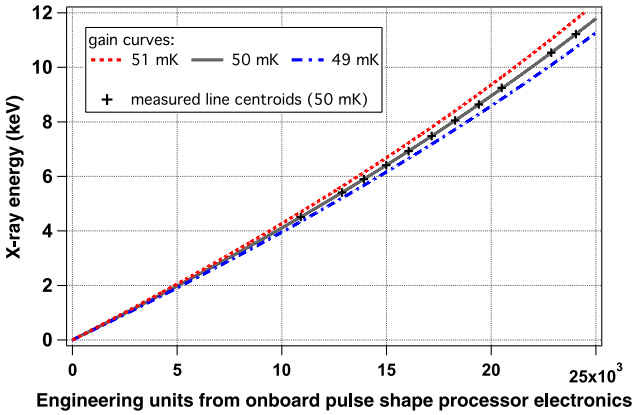

Fig. 16 Gain scales for a single SXS pixel at three heat-sink temperatures, used to relate measured x-ray signal to absolute x-ray energy for hi-res events. The black symbols (+) provide an example of the line-centroid data we fit to generate each gain curve. In nominal He operation mode, the gain was well described by the 50 mK curve, whereas the 49 and 51 mK gain scales bound the gain conditions we expected to encounter on orbit.

different pixel temperature or radiative loading of the pixels themselves. We could not simply assume that each pixel was at the same temperature as the reading on the control thermometer.

As a result, we use the following approach. We measured gain curves at three heat-sink temperatures, with the intention that the resulting gain curves will envelope the gain curves we were apt to encounter during the mission lifetime. These curves were then used in the mission software pipeline,[42] in conjunction with a fiducial line measured onboard, to construct a gain curve appropriate for the instantaneous operating conditions of the instrument. Reference 43 provides details about this nonlinear drift correction approach, including analyses highlighting our ability to recover x-ray energies to better than 1 eV over the SXS science bandpass even for large-scale gain variations, easily meeting the ± 2 eV calibration requirement.

Figure 16 shows an example of SXS gain curves at heat-sink temperatures of 49, 50, and 51 mK. Under nominal operating conditions, the instrument gain was very close to the 50 mK calibration curve.

4.3.2 *Details of gain scale calibration data acquisition*

The calibration measurements of the SXS detector gain were performed in March 2015 during SXS instrument-level testing at Tsukuba Space Center using the flight version of the electronics boxes (XBOX, ADRC). The SXS dewar was in its final flight configuration, following the installation of the isolators between the dewar and the cryocoolers.[44] Figure 17 shows a photo of the experimental setup, and Table 7 lists key instrument parameters. We used the RTS positioned above the dewar to provide x-ray lines at known energies from 4.5 to 13.5 keV. For the case of the gain measurements, we used the following targets in the eight slots: (0) Fe, (1) KBr, (2) Cu, (3) GaAs, (4) Co, (5) Cr, (6) Mn, and (7) TiO_2. The x-ray source settings were adjusted to provide of order 1 ct/s/pixel, and the dwell time at each target ranged from 10 to 70 s. The total exposure time for each gain scale measurement was 8 to 12 h.

Data were acquired using the PSP. The pulse height amplitude (PHA) for hi-res events was calculated using a 1024-sample optimal filter, whereas mid-res PHAs were calculated using a 256-sample optimal filter. Each pixel had a hi-res and mid-res optimal filter template stored onboard,

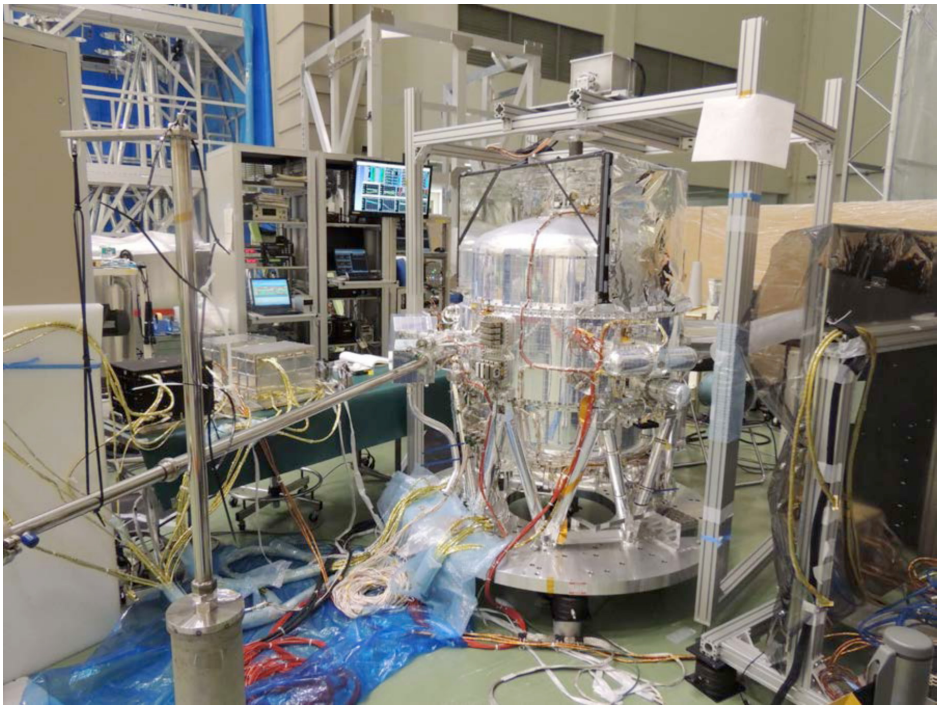

Fig. 17 RTS mounted above the SXS during the instrument-level calibration campaign at Tsukuba Space Center in March 2015.

Table 7 Selected instrument parameters during SXS gain calibration.

		Comments
PSP parameters		
Trigger thresholds	≈25 (=32 eV)	5σ per-pixel thresholds[a]
Templates	SHPTEMPL = March 10, 2015	
Average pulse scale	144,000	PSP parameter PHA_AVGPULSE
Software version	$0 \times 150,310$	
XBOX parameters		
Detector bias setpoint	1.60784 V	0×0052 in hex
Detector bias readback	1a = 1.582 V, 1b = 1.585 V, 1c = 1.583 V, 1d = 1.588 V	
ADRC parameters and relevant temperatures		
CTS temperature setpoint	49.0/50.0/51.0 mK	Cryogen mode operation
Control thermometer	CT0 Sensor0	
DA temperature	1.220 to 1.32 K	
He tank temperature	1.216 to 1.227 K	
IVCS temperature	26.5 to 26.9 K	

[a]Thirty of the pixels had thresholds of 24 to 26; the others were between 28 and 62. See Ref. 32 for a complete list of the thresholds used during the March 2015 Tsukuba calibration campaign.

and a given set of these 72 filter templates were identified by the SHPTEMPL keyword. The optimal filter templates were calculated during the calibration phase in March 2015, and assigned SHPTEMPL = 2015-03-10, as described in Ref. 32.

Lo-res events were not optimally filtered in the PSP; instead their pulse height was given by the maximum value in analog-to-digital units (ADU) in the sample record (after subtracting the baseline value of the sample). In fact, this lo-res pulse height (LO_RES_PHA) was calculated not just for lo-res events but for events of all grades, so we acquired simultaneous lo-res gain scale information during experiments aimed at calibrating hi-res or mid-res event grades.

To acquire spectra for the hi-res and lo-res gain scales, we operated the PSP in its normal mode. For the hi-res gain scale, we derived curves by relating the PHA to x-ray energy using hi-res events. For the lo-res gain scale, we used all primary events (hi-res, mid-res primaries, and lo-res primaries) but relate the LO_RES_PHA to x-ray energy.

To obtain a sufficient number of mid-res events in a reasonable exposure time, both for the case of our relatively low count-rate energy scale calibration setup at Tsukuba and as was planned for appropriate celestial sources, we operated the PSP in forced mid-res mode. In this mode, hi-res-graded events were processed as if they were mid-res (using the 256-sample optimal filter template) so that both hi-res and mid-res events could be combined to measure a mid-res gain scale by relating the PHA to x-ray energy. Prior to the calibration campaign, we verified that these forced mid-res events are equivalent to mid-res primaries acquired in the normal operating mode, both with respect to the gain scale and resolution at 6 keV.

4.3.3 *Gain scale data analysis*

For each experiment, we followed a standard procedure to determine the detector gain curve. The following prescription was performed independently for each of the array pixels. First, we applied a linear drift correction to the data, if necessary, to remove very small changes in effective detector temperature over the course of the exposure. Next, we made histograms of the events using a bin width of ∼1 ADU (∼0.5 eV). We then fit each of the x-ray line complexes to determine a set of PHA–energy pairs and associated error estimates. Finally, we fit these data to a fourth-order polynomial.

For each of the three heat-sink temperatures, we made spectra for each pixel using hi-res events. We fit the following line complexes: Ti Kα, Cr Kα, Mn Kα, Fe Kα, Co Kα, Cu Kα, Ga Kα, As Kα, and Br Kα. One exception is the calibration pixel (pixel 12). Since it only received photons from the collimated ^{55}Fe source, not from the instrument aperture, we derived its gain scale from fits to two only line complexes, Mn Kα and Kβ. Therefore, we constrained the pixel 12 fit functions to a second-order polynomial.

We acquired data at 50 mK in forced mid-res mode, in which both hi-res and mid-res events are processed with the 256-sample (mid-res) optimal filter template, allowing much more efficient data collection for mid-res-processed pulses. We use the same set of x-ray line complexes as described for the hi-res gain. A linear stretch (∼0.9998) was applied to the resulting 50 mK mid-res gain scales to correct for a slight difference in the effective temperature during the forced mid-res exposure as compared with the 50 mK hi-res exposure.

We did not have time to acquire data in forced mid-res mode at 49 and 51 mK prior to delivery to the spacecraft. Instead, we calculated the gain components by scaling the 50 mK mid-res gain curve by the ratio of the 49 mK (or 51 mK) hi-res gain curve to the 50 mK hi-res gain curve, and then fitting a fourth-order polynomial to the resulting curve. We tested the efficacy of this approach by evaluating the (low-statistics) mid-res primary lines obtained during the 49/51 mK hi-res experiments and found that the results give errors of <5 eV at 49 mK and <10 eV at 51 mK. These were deemed acceptable for nominal cryogen mode observations since we operate very close to the 50 mK gain curves, but were planned to be re-measured on orbit if necessary.

We used the LO_RES_PHA of primary events of all grades and fit the same set of lines to determine the gain curves at each temperature. Since the lo-res data were acquired simultaneously with the hi-res data, the reference effective temperature for each dataset was by definition the same and did not require additional corrections (as in the case of the mid-res data).

We planned to check the SXS gain during the in-flight calibration phase using a combination of onboard sources and celestial sources for a set of operating conditions (49, 50, 51 mK; and in forced mid-res mode at each temperature). Our aim was to have parameterized the gain on the ground in such a way that even if operating conditions were slightly different on orbit, the change in gain would be wholly described by a change in effective temperature, and would not require an update to the gain calibration files used for data analysis. However, we did

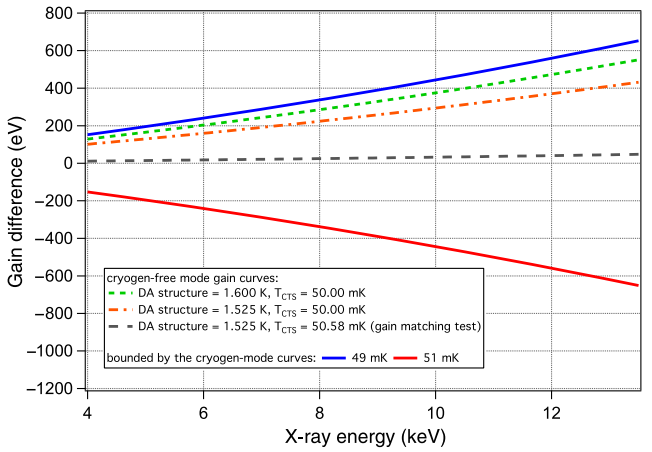

Fig. 18 Gain difference between labeled curves and the cryogen mode 50-mK gain curve, each for a single SXS pixel (pixel 11). The plot illustrates that the 49- and 51-mK cryogen-mode gain curves enveloped the cryogen-free mode gain curves, as was required for our nonlinear drift correction approach. In cryogen-free mode, the DA structure temperature was at a higher temperature (1.525 to 1.600 K) than it was in cryogen mode (1.22 K). In a subsequent test, we adjusted the control point for the CTS temperature to 50.58 mK so that the gain curve with the DA structure temperature at 1.525 K was similar to that during nominal cryogen-mode operating conditions.

expect that the addition of low-energy lines in the gain calibration measurements as well as the forced mid-res data at 49 and 51 mK might have required an update to these files.

In addition to the data used to create the gain curves described above, we also performed similar measurements in cryogen-free mode[26] with several combinations of CTS control temperature, DA structure control temperature, and IVCS temperature (see Fig. 18). These measurements were essential in verifying our approach and confirming that the 49/51 mK cryogen-mode data enveloped the gain conditions encountered in cryogen-free mode. We also acquired ground calibration data at Tsukuba and at GSFC over an extended energy bandpass—to energies of 25 and 30 keV, respectively. These data could have been incorporated at a later stage if deemed necessary. Figure 19 shows the magnitude of gain errors that will arise above ~12 keV due to our not including the high-energy measurements in the prelaunch best-estimates of the gain coefficients.

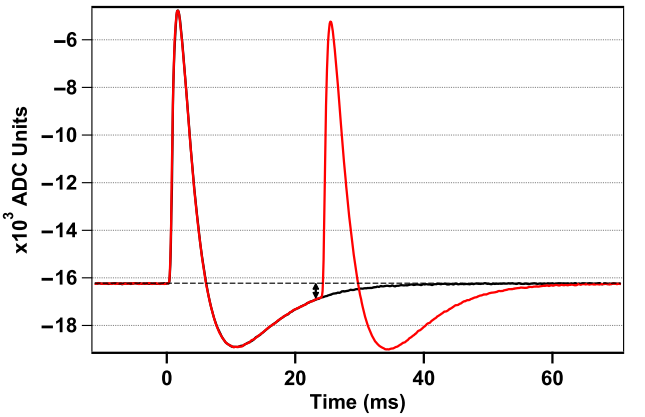

Fig. 20 An example of a mid-res secondary event (right pulse) following a mid-res primary of the same energy (left pulse). The black underlying curve shows a hi-res pulse for comparison. The PSP determines the PHA of the mid-res secondary pulse by fitting the optimal filter template without subtracting the preceding pulse waveform, leading to an underestimated PHA as the secondary starts on the undershoot of the previous pulse. The vertical arrow and dashed line highlight the origin of the term we must correct, which is dependent on the difference in event arrival times.

4.3.4 *Gain correction for mid-res secondaries*

For each mid-res secondary event, we apply a correction factor to the PHA before gain correction.[45] This additional factor depends on the time between the primary and secondary pulses, and the energy of the primary pulse. Figures 20 and 21 show our approach.

We find that the functional form of the correction is well described by the pulse shape of the average hi-res pulse. Because the detector pulse shape depends on energy we constructed a set of 10 normalized average pulse shapes for each detector pixel using hi-res data for incident x-ray energies ranging from 4.5 keV (Ti Kα) to 11.9 keV (Br Kα) using the RTS data described in Sec. 4.3.2. For the calibration pixel, we calculated only two average pulse shapes using Mn Kα and Kβ photons from the ^{55}Fe source. These pulse shapes are used as a look-up table for the PHA adjustment. When a mid-res primary has multiple secondaries, the correction term must be calculated and applied to each secondary, starting with the

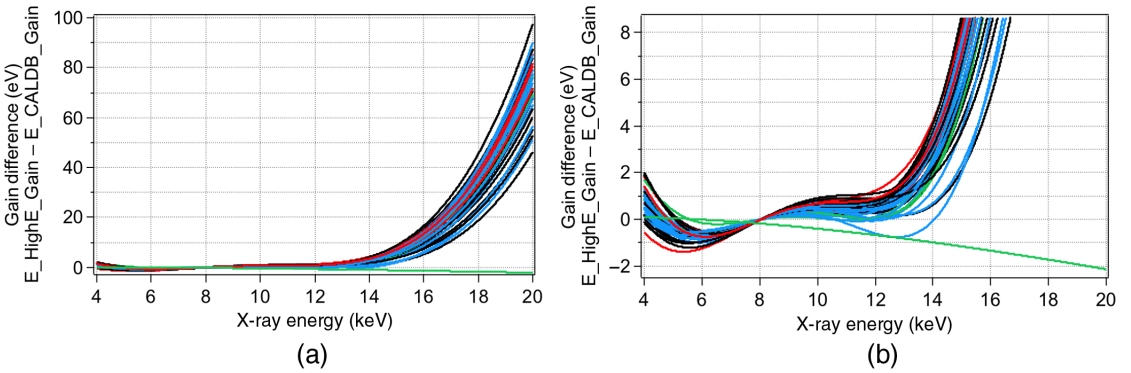

Fig. 19 (a) The difference in derived event energy using the high-energy gain coefficients derived using data to 25 keV compared with the nominal gain coefficients for the 36 SXS pixels. The gain will be underestimated by 45 to 100 eV at 20 keV. The green curve is the calibration pixel. (b) Zoom showing that the gain scales agree to within $\sim \pm 1$ eV for x-ray energies up to 13 keV.

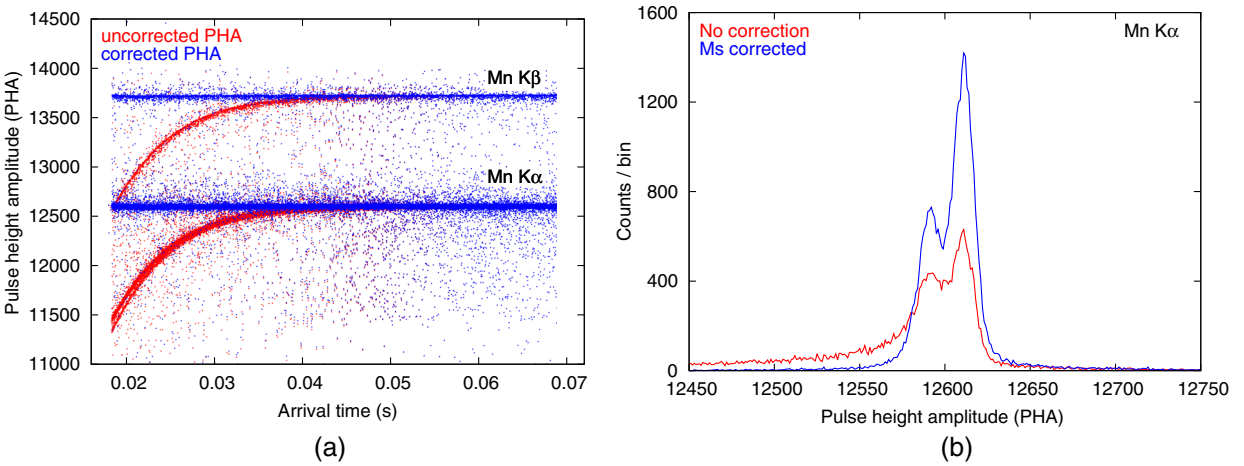

Fig. 21 (a) Comparison of mid-res secondary PHA before and after correction at Mn Kα (5.898 keV) and Mn Kβ (6.4 keV). Each dot represents a mid-res secondary event PHA as a function of arrival time relative to the primary event's arrival time. The two branches of the bottom left red "curve" indicate Mn Kα secondaries with Mn Kα primaries (top branch) and Mn Kβ primaries (bottom branch). (b) Histogram of mid-res secondaries at Mn Kα before and after correction. The correction significantly improves the spectral resolution and reduces the line distortion.

event closest in time to the primary, using $\mathrm{PHA1}_{\mathrm{corr}} = \mathrm{PHA1} - P_i(t_1 - t_0 + t_{\mathrm{offset}}) * \mathrm{PHA0}/32767$, where PHA1 is the PHA of the secondary as calculated by the PSP, PHA0 is the adjusted PHA of the preceding event (for the primary event PHA0 does not need adjustment), P_i is the normalized average pulse shape for the appropriate energy range, which is evaluated at the bin given by the difference in the secondary and its preceding event arrival time $(t_1 - t_0)$ shifted by t_{offset} (offset to the peak of the average pulse). Reference 45 presents a more detailed description of the CALDB file and correction procedure. To give an idea of the magnitude of the improvement using data from the calibration pixel, we found that the correction improved the energy resolution of mid-res secondaries from ~7.6 to 5.9 eV FWHM for the case, where the resolution for mid-res primaries was 4.7 eV FWHM.

5 Anti-coincidence Detector Calibration

A fraction of cosmic rays that traverse the SXS pixels will leave behind energy comparable to photons in the SXS bandpass. An anti-co detector sat behind the detector array to enable rejection of cosmic ray events as well as to provide an independent monitor of the particle background. The SXS anti-co was a silicon ionization detector with a temperature invariant gain. The anti-co was 0.5-mm thick with an area of 1 cm^2 (4 times larger than the detector array) and a time constant of 0.15 ms (tuned to be ~23 times shorter than the microcalorimeter pixel fall times). There was a single anti-co detector, but, for redundancy, it was read out using two separate readout chains. An overview of the anti-coincidence detector appears in the Astro-E2 instrument paper[46] and the changes made to the anti-co readout for Astro-H are reported in Ref. 6. Additional detail about the SXS anti-co, including a schematic of the detector array and anti-co plus the events observed in both due to the in-orbit particle background, may be found in Ref. 40.

We calibrated the anti-co energy gain scale, which is used to convert anti-co events from PHA to energy, in January 2015, during SXS instrument-level testing at Tsukuba. We used the RTS positioned above the dewar to provide x-ray lines at known energies. For the case of the anti-co gain measurement, we used the RTS in nonrotating mode to provide a constant flux of x-rays at 22.105 keV (Ag Kα_{12}) and 24.94 keV (Ag Kβ) for a total of 1.5 h. The instrument was in a nominal operating state with a detector temperature of 50 mK and an anti-co bias of 6 V for each channel. These data were acquired prior to installation of the isolators between the dewar and the cryocoolers,[44] but this difference should not affect the anti-co gain.

Data were acquired using the PSP. The anti-co signal was read out on one A-side channel and one B-side channel.[32] The PSP calculated the PHA of each anti-co event onboard by subtracting the anti-co pedestal from the raw pulse height (the maximum sample for each triggered event). The anti-co pedestal is a commandable value that was determined in previous ground testing to "zero" the anti-co PHA, so that histograms of anti-co baseline events are centered at the origin. For the A-side anti-co, the pedestal was −6613 ADU and trigger threshold was 15 ADU; the B-side settings were −6611 ADU and 15 ADU. We did not plan to change the pedestal settings during the mission lifetime. See Ref. 32 for further details of the PSP operating parameters.

The anti-co detector was known to be linear[6] over its operating bandpass of ~1 keV to 6 MeV, and thus we parameterize the gain as $E[\mathrm{keV}] = c_0 + c_1 * \mathrm{PHA}$. The offset coefficient (c_0) is included to correct any sub-ADU shift in the zero-point, which was likely since the pedestal is limited to an integral number of ADU.

Figure 22 shows the anti-co spectrum for the A-side anti-co (called channel 0 in the mission analysis software). To derive the anti-co gain, we require a precise measure of the centroid of the Ag Kα complex. Because the anti-co resolution was ~1.7 keV FWHM, the Ag Kα line is blended with the Ag Kβ line. Instead of a simple Gaussian fit, we performed a two-Gaussian fit to the Ag Kα and Kβ region. We found that the resulting fit was skewed by the counts at lower energy (from 15 to 40 ADU), and thus added an empirical model of the low-energy continuum to the fit function (blue curve). We also fit the anti-co baseline events to determine the sub-ADU offset parameter. We find that each anti-co channel has a scaling of 0.420 keV per ADU, which is consistent with gain scale measurements taken during subsystem testing at GSFC using

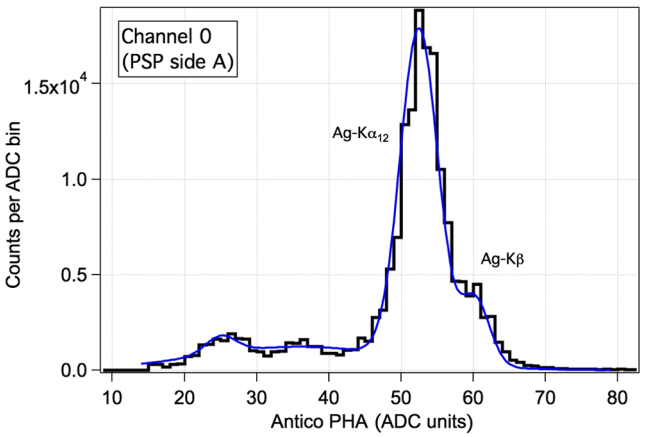

Fig. 22 Anti-co channel 0 spectrum (black histogram) and corresponding fit (blue curve). These data were used to determine the anti-co gain scale parameters.

Table 8 SXS anti-co detector gain coefficients, valid over the operating range of ~1 keV to 6 MeV. The uncertainty on the offset values is ~0.02 keV; the uncertainty on the scaling terms is ~0.001 keV/ADU. We expected that these gain coefficients would have been valid for the entirety of the mission.

	Anti-co gain parameters	
Anti-co channel ID	c_0 [keV]	c_1 [keV/ADU]
0 (PSP side A)	0.0462	0.420
2 (PSP side B)	0.3486	0.420

^{241}Am to provide ~60 keV photons and checks of the gain scale using Ag photons during instrument-level testing in March 2015, after installation of the SXS isolators[44] (final flight configuration of the instrument). Table 8 shows the anti-co gain parameters.

The anti-co lines showed an asymmetric distribution, with a tail to low energy, due to an arrival-time—PHA dependence. This asymmetry was not apparent at low energies (e.g., at Ag Kα) but became more pronounced at higher energies. Thus a simple PHA—energy gain conversion becomes less well defined at higher energies; however, the only requirement on the knowledge of the anti-co energy scale was to provide knowledge of the energy and resolution near the threshold, which was typically set at ~10 keV. Having information about the rest of the spectrum was expected to be an interesting diagnostic, but there was no such instrument calibration requirement.

6 Brief Summary of Timing Calibration

For the SXS, the timing calibration data are used in the software pipeline's time assignment process,[39,42] both for the detector pixels and anti-co channels, as well as to study the relative timing between various classes of events to derive screening criteria, which include background particle events, electrical cross talk, and other correlated events. The timing calibration depends upon the event grade: for hi-res and mid-res events it depends on the optimal filter and the trigger threshold used when creating the optimal filter template, whereas for the lo-res events the initial time assignment is performed using a hardware-determined local time counter. The timing coefficients were derived on the ground, and then updated using on-orbit data. Reference 33 will describe details of the timing calibration and Ref. 40 discusses the origin of the background events. Here we provide a brief summary.

Using the EM MXS mounted directly above the dewar during instrument-level calibration (see Sec. 4.1.5), we measured the relative timing coefficients, highlighting the difference in timing coefficients required on the pixels that had much higher trigger thresholds. We also performed studies of the timing of cross-talk events.

During spacecraft-level testing, we performed several parts of the timing calibration. We used the onboard MXSs operated in pulsed mode to measure the position of the leading edge of the phase-folded data for each pixel for each event grade, from which we derived coefficients needed in the process of converting trigger time to Universal Time. Due to uncertainties in the time delay between the commanded MXS flash "on" time and the emission of photons, there remained ambiguity in this time tagging. A more thorough calibration of the MXS timing itself would have eliminated this ambiguity, but this was not pursued during subsystem testing and instead we had to rely on astronomical sources for absolute timing calibration. For future missions, we aim to better characterize the MXS timing properties to increase our knowledge of the detection chain timing prior to launch.

We also acquired "background" datasets ($\gtrsim$12 h exposures with no external x-ray source) to study the relative timing between the array events and anti-coincidence detector signals caused by atmospheric muons. We used data with low (~25) trigger thresholds to refine the study of electrical cross-talk data and with high (~120) thresholds to study the timing of correlated events caused when a photoelectron was lost from one pixel and absorbed by another. These data used both the FW ^{55}Fe source and the MXS; because of the GV shadowing of the MXS most pixels received photons only from the ^{55}Fe source.

7 Summary

The Astro-H SXS ground calibration campaign included a careful characterization and calibration of the optical blocking filters and detector system. The transmission of the set of five optical blocking filters was modeled based on synchrotron measurements. The detector system calibration campaign focused on measuring and understanding the line-spread function for incident x-ray energies from 0.3 to 12 keV as well as the energy gain scale and its parametrics. Each of these detector system parameters require individual calibration terms for each of the 36 microcalorimeter pixels. These parameters, in conjunction with onboard sources, were successfully used to calibrate the instrument during the mission lifetime.[4,24,47]

Acknowledgments

We gratefully acknowledge the Luxel Corporation, including T. Ayers, B. Lairson, and H. Lopez; the NSLS beamline staff, including B. Dong; the NNSA Participating Research Team (LANL, LLNL, NSTec, and SNL), including K. Moy and F. Weber; the CLS beamline staff, including S. Urquhart and J. Wang; L.C. Gallo; N. Hell; L. Kolos; K. Kripps; S.E. Busch; and J.-P. Porst for support during the development and calibration of the optical blocking filters. We thank T. Coffroad, S.J. Moseley, and T. Okajima for support in the design and

preparation of detector calibration equipment, and M.C. Witthoeft for support of the gain correction for mid-res secondaries. And finally, we thank all of the US, Japanese, and European SXS team members who contributed to the years of development and testing at GSFC, Niihama, Tsukuba, and Tanegashima, including the postdocs and students who supported the long series of tests at Niihama and Tsukuba. The optical blocking filters calibration used beamlines X8A and U3C of the National Synchrotron Light Source, a U.S. Department of Energy (DOE) Office of Science User Facility operated for the DOE Office of Science by Brookhaven National Laboratory under Contract No. DE-AC02-98CH10886. Additional measurements were performed at the Canadian Light Source, which is supported by the Natural Sciences and Engineering Research Council of Canada, the National Research Council Canada, the Canadian Institutes of Health Research, the Province of Saskatchewan, Western Economic Diversification Canada, and the University of Saskatchewan. The synchrotron radiation experiments of the spare gate valve Be window were performed at BL01B1 of SPring-8 with the approval of the Japan Synchrotron Radiation Research Institute (JASRI) (Proposal No. 2016A1864). We acknowledge Tomoya Uruga and Toshiaki Ina at JASRI for the measurements and Yoshitomo Maeda at ISAS for support. This article is based on a paper presented at the SPIE Astronomical Telescopes and Instrumentation conference, 26 June to 1 July 2016, in Edinburgh. Scotland,[18]

References

1. T. Takahashi et al., "The ASTRO-H X-ray astronomy satellite," *Proc. SPIE* **9144**, 914425 (2014).
2. T. Takahashi et al., "The ASTRO-H (Hitomi) x-ray astronomy satellite," *J. Astron. Telesc., Instrum., Syst.* **4**(2), 021402 (2018).
3. R. L. Kelley et al., "The Astro-H high resolution soft x-ray spectrometer," *J. Astron. Telesc., Instrum., Syst.* (2018).
4. Hitomi Collaboration, "The quiescent intracluster medium in the core of the Perseus cluster," *Nature* **535**, 117–121 (2016).
5. M. Tsujimoto et al., "In-orbit operation of the soft x-ray spectrometer onboard the Hitomi satellite," *J. Astron. Telesc., Instrum., Syst.* **4**(1), 011205 (2017).
6. C. A. Kilbourne et al., "The design, implementation, and performance of the Astro-H SXS calorimeter array and anti-coincidence detector," *J. Astron. Telesc., Instrum., Syst.* **4**(1), 011214 (2018).
7. C. A. Kilbourne et al., "The design, implementation, and performance of the Astro-H SXS aperture assembly and blocking filters," *J. Astron. Telesc., Instrum., Syst.* **4**(1), 011215 (2018).
8. R. Iizuka et al., "Ground-based x-ray calibration of the Astro-H soft x-ray telescopes," *Proc. SPIE* **9144**, 914458 (2014).
9. T. Okajima et al., "First peek of Astro-H soft x-ray telescope (SXT) in-orbit performance," *Proc. SPIE* **9905**, 99050Z (2016).
10. M. Tsujimoto et al., "In-flight calibration of Hitomi soft x-ray spectrometer (3) effective area," *Publ. Astron. Soc. Jpn.* (2018).
11. B. L. Henke, E. M. Gullikson, and J. C. Davis, "X-ray interactions: photoabsorption, scattering, transmission, and reflection at E = 50-30, 000 eV, Z = 1-92," *At. Data Nucl. Data Tables* **54**, 181–342 (1993).
12. D. L. Perry and S. L. Phillips, *Handbook of Inorganic Compounds*, CRC Press, Boca Raton (2000).
13. "CXRO atomic scattering factor files," http://henke.lbl.gov/optical_constants/asf.html (01 November 2015).
14. "NIST x-ray form factor, attenuation, and scattering tables," http://www.nist.gov/pml/data/ffast/index.cfm (01 November 2015).
15. C. T. Chantler, "Theoretical form factor, attenuation, and scattering tabulation for Z = 1-92 from E = 1-10 eV to E=0.4-1.0 MeV," *J. Phys. Chem. Ref. Data* **24**, 71–643 (1995).
16. C. T. Chantler, "Detailed tabulation of atomic form factors, photoelectric absorption and scattering cross section, and mass attenuation coefficients in the vicinity of absorption edges in the soft X-Ray (Z = 30-36, Z = 60-89, E = 0.1 keV-10 keV), addressing convergence issues of earlier work," *J. Phys. Chem. Ref. Data* **29**, 597–1056 (2000).
17. "Hitomi CALDB documents," http://heasarc.gsfc.nasa.gov/docs/hitomi/calib/hitomi_caldb_docs.html (01 July 2016).
18. M. E. Eckart, M. A. Leutenegger, and the SXS Instrument Team, "Ground calibration of the Astro-H (Hitomi) soft x-ray spectrometer," *Proc. SPIE* **9905**, 99053W (2016).
19. M. E. Eckart and M. A. Leutenegger, and the SXS Instrument Team, "Instrument calibration report, SXS gate valve window transmission, ASTH-SXS-CALDB-GATEVALVE," 2016, http://heasarc.gsfc.nasa.gov/docs/hitomi/calib/hitomi_caldb_docs.html (01 July 2016).
20. T. Yaqoob, "Instrument calibration report, SXS gate valve and filter wheel filters, ASTH-TEL-CALDB-FILT," 2016, http://heasarc.gsfc.nasa.gov/docs/hitomi/calib/hitomi_caldb_docs.html (01 July 2016).
21. A. Hoshino et al., "The evaluation of the Hitomi (Astro-H)/SXS spare beryllium window in 3.8-30 keV," *Proc. SPIE* **10397**, 103970E (2017).
22. "Online Bragg planes calculator," http://x-server.gmca.aps.anl.gov/x0h_search.html (20 October 2016).
23. Y. Yoshida et al., "Transmission measurement of the spare Beryllium window of the SXS onboard the Hitomi satellite in 2.0–12 keV with KEK-PF," *Proc. SPIE* **10397**, 103971D (2017).
24. M. A. Leutenegger et al., "In-flight verification of the calibration and performance of the ASTRO-H (Hitomi) soft x-ray spectrometer," *J. Astron. Telesc., Instrum., Syst.* **4**(2), 021407 (2018).
25. C. P. de Vries et al., "Calibration sources and filters of the soft x-ray spectrometer instrument on the Hitomi spacecraft," *J. Astron. Telesc., Instrum., Syst.* **4**(1), 011204 (2017).
26. G. A. Sneiderman et al., "Cryogen-free operation of the soft x-ray spectrometer instrument," *Proc. SPIE* **9905**, 99053N (2016).
27. S. Takeda et al., "Performance verification and system integration tests of the pulse shape processor for the soft x-ray spectrometer onboard ASTRO-H," *Proc. SPIE* **9144**, 91445B (2014).
28. Y. Shimoda et al., "Development of a digital signal processing system for the x-ray microcalorimeter onboard ASTRO-H (II)," *J. Low Temp. Phys.* **167**, 575–581 (2012).
29. H. Seta et al., "The digital processing system for the soft x-ray spectrometer onboard ASTRO-H—the design and the performance," *IEEE Trans. Nucl. Sci.* **59**, 366–372 (2012).
30. A. E. Szymkowiak et al., "Signal processing for microcalorimeters," *J. Low Temp. Phys.* **93**, 281–285 (1993).
31. K. R. Boyce et al., "Design and performance of the ASTRO-E/XRS signal processing system," *Proc. SPIE* **3765**, 741–750 (1999).
32. Y. Ishisaki et al., "In-flight performance of pulse processing system of the ASTRO-H soft x-ray spectrometer," *J. Astron. Telesc., Instrum., Syst.* **4**(1), 011217 (2018).
33. S. Koyama et al., "In-orbit timing calibration of SXS, HXI and SGD on board Hitomi," in preparation (2018).
34. M. C. Hettrick, "Surface normal rotation: a new technique for grazing-incidence monochromators," *Appl. Opt.* **31**, 7174–7177 (1992).
35. M. A. Leutenegger et al., "Compact, low-cost, high-resolution monochromatic x-ray source for characterization of x-ray calorimeter arrays," in preparation (2018).
36. M. P. Chiao et al., "System design and implementation of the detector assembly for the Astro-H soft x-ray spectrometer," *J. Astron. Telesc., Instrum., Syst.* **4**(2) 021404 (2018).
37. C. P. de Vries et al., "Calibration sources for the soft x-ray spectrometer instrument on ASTRO-H," *Proc. SPIE* **8443**, 844353 (2012).
38. M. A. Leutenegger et al., "In-flight calibration of Hitomi soft x-ray spectrometer (5) RMF," in preparation (2018).
39. M. Tashiro et al., "Instrument calibration report, SXS timing coefficients, ASTH-SXS-CALDB-COEFTIME," 2016, http://heasarc.gsfc.nasa.gov/docs/hitomi/calib/hitomi_caldb_docs.html (15 January 2018).
40. C. A. Kilbourne et al., "In-flight calibration of Hitomi soft x-ray spectrometer (1) background," *Publ. Astron. Soc. Jpn.* (2018).
41. M. A. Leutenegger et al., "Instrument calibration report, SXS response matrix, ASTH-SXS-CALDB-RMFPARAM," 2016, http://heasarc.gsfc.nasa.gov/docs/hitomi/calib/hitomi_caldb_docs.html (09 July 2016).
42. L. Angelini et al., "Astro-H data analysis, processing and archive," *J. Astron. Telesc., Instrum., Syst.* **4**(1), 011207 (2018).
43. F. S. Porter et al., "Temporal gain correction for x-ray calorimeter spectrometers," *J. Low Temp. Phys.* **184**, 498–504 (2016).

44. Y. Takei et al., "Vibration isolation system for cryocoolers of soft x-ray spectrometer onboard ASTRO-H (Hitomi)," *J. Astron. Telesc., Instrum., Syst.* **4**(4), 011216 (2018).
45. M. P. Chiao et al., "Instrument calibration report, SXS Mid Res secondary PHA correction, ASTH-SXS-CALDB-SECPULSE," 2017, http://heasarc.gsfc.nasa.gov/docs/hitomi/calib/hitomi_caldb_docs.html (09 July 2017).
46. R. L. Kelley et al., "The Suzaku high resolution x-ray spectrometer," *Publ. Astron. Soc. Jpn.* **59**, S77–S112 (2007).
47. F. S. Porter et al., "In-flight performance of the soft x-ray spectrometer detector system on Astro-H," *J. Astron. Telesc., Instrum., Syst.* **4**(1), 011218 (2018).

Megan E. Eckart is a research astrophysicist in the X-ray Microcalorimeter Group at NASA's Goddard Space Flight Center.

Biographies for the other authors are not available.